The potential role of NGC 205 in generating Andromeda's vast thin corotating plane of satellite galaxies

Garry W. Angus,[1,2]★ Paul Coppin,[2] Gianfranco Gentile[3,2] and Antonaldo Diaferio[4,5]

[1]*Department of Physics and Astronomy, Botswana International University of Science and Technology, Plot 10071, Private Bag 16, Palapye, Botswana*
[2]*Department of Physics and Astrophysics, Vrije Universiteit Brussel, Pleinlaan 2, B-1050 Brussels, Belgium*
[3]*Sterrenkundig Observatorium, Universiteit Gent, Krijgslaan 281, B-9000 Gent, Belgium*
[4]*Dipartimento di Fisica, Università di Torino, Via P. Giuria 1, I-10125 Torino, Italy*
[5]*Istituto Nazionale di Fisica Nucleare, Via P. Giuria 1, I-10125 Torino, Italy*

ABSTRACT

The Andromeda galaxy is observed to have a system of two large dwarf ellipticals and $\sim$13 smaller satellite galaxies that are currently corotating in a thin plane, in addition to 2 counter-rotating satellite galaxies. We explored the consistency of those observations with a scenario where the majority of the corotating satellite galaxies originated from a subhalo group, where NGC 205 was the host and the satellite galaxies occupied dark matter sub-subhaloes. We ran N-body simulations of a close encounter between NGC 205 and M31. In the simulations, NGC 205 was surrounded by massless particles to statistically sample the distribution of the sub-subhaloes expected in a subhalo that has a mass similar to NGC 205. We made Monte Carlo samplings and found that, using a set of reference parameters, the probability of producing a thinner distribution of sub-subhaloes than the observed NGC 205 + 15 smaller satellites (thus including the two counter-rotators, but excluding M32) increased from $<10^{-8}$ for the initial distribution to $\sim10^{-2}$ at pericentre. The probability of the simulated sub-subhaloes occupying the locations of the observed corotating satellites in the line-of-sight velocity versus projected on-sky distance plane is at most 2×10^{-3} for 11 out of 13 satellites. Increasing the mass of M31 and the extent of the initial distribution of sub-subhaloes gives a maximum probability of 4×10^{-3} for all 13 corotating satellites, but the probability of producing the thinness would drop to $\sim10^{-3}$.

Key words: methods: numerical – galaxies: kinematics and dynamics – Local Group – dark matter.

1 INTRODUCTION

In the concordance cosmological model (Davis et al. 1985; Frenk et al. 1985, 1988; Spergel et al. 2007; Planck Collaboration XVI 2014), large spiral galaxies, like the Milky Way (MW) and Andromeda (M31), form in an expanding universe through the aggregation of cold dark matter around an initial seed overdensity (White & Rees 1978; White & Frenk 1991). The smallest scale perturbations attract the surrounding matter in the shortest time-scale and thus form their haloes first. Owing to the higher background density at earlier times, these small haloes are more dense than their larger counterparts. They are eventually encompassed by larger haloes and some are destroyed by tidal forces causing their dark matter to be dispersed throughout the smooth component of the larger halo. A portion survive the tidal forces and can be labelled subhaloes.

The Aquarius project (Springel et al. 2008) is one of the largest cosmological N-body simulations of MW/Andromeda-sized dark matter haloes, with a thorough investigation of subhalo statistics. According to their simulations, these subhaloes have a more extended distribution around the host halo than the smooth component. This is inevitable since the subhaloes at great distances from the host halo experience weaker tides and are therefore less prone to the culling that the subhaloes on short radius orbits encounter. The mass function of subhaloes surrounding the host halo can, on average, be represented by a power law $dn/dm \propto m^{-1.9}$ and typically the most massive subhaloes are around 1/100th the mass of the host. Those most massive subhaloes also tend to lie beyond the virial radius of the host.

These massive subhaloes can also play host to sub-subhaloes (see Diemand, Kuhlen & Madau 2007), which are haloes that are bound primarily to the subhalo. The mass function of these sub-subhaloes is similar to that of the subhaloes, albeit with a slightly lower normalization, meaning fewer total satellites per decade of

★ E-mail: angus.gz@gmail.com

mass. The distribution of the sub-subhaloes has not been precisely quantified and although it may be similar to that of the subhaloes, its extent is likely truncated given the tidal forces of the host halo (which can sunder the sub-subhalo from the subhalo). In addition, sub-subhaloes cannot be replenished.

It is well known that only a fraction of the possible subhaloes of the MW and M31 host satellite galaxies (Klypin et al. 1999; Moore et al. 1999). Furthermore, some of the most massive predicted subhaloes of those two large galaxies do not have corresponding stellar (luminous) counterparts. This means the bright satellite galaxies of the MW and M31 are hosted by subhaloes that are much less massive than the most massive ones. This contradiction is known as the too big to fail (TBTF) problem (Boylan-Kolchin, Bullock & Kaplinghat 2011, 2012; Garrison-Kimmel et al. 2013, 2014b). In essence, if a low-mass subhalo is able to accrete gas and form stars with its puny potential well, then so should a more massive subhalo.

A further complication is that roughly half of the detected satellite galaxies orbiting M31 (see e.g. Koch & Grebel 2006; McConnachie 2012; Conn et al. 2013) lie in a highly flattened plane and the majority of those (14 out of 16) have a common sense of rotation (Ibata et al. 2013) – dubbed the vast thin corotating (hereafter VTC) plane of satellites. This highly organized distribution is unlikely to be the result of stochastic star formation in certain subhaloes (Walker & Loeb 2014 and Ibata et al. 2014b in response to Bahl & Baumgardt 2014). As it happens, the MW has a similar satellite distribution where most satellite galaxies could be part of a highly extended and flattened disc – some 300 kpc in radius with a root mean squared (rms) thickness of merely 30 kpc (Lynden-Bell 1983; Metz, Kroupa & Libeskind 2008; Kroupa et al. 2010; Pawlowski, McGaugh & Jerjen 2015; Pawlowski 2016). Unfortunately, the difficulties involved with measuring proper motions make it challenging to determine if the satellites are corotating.

A matter of current debate in the literature is whether corotating planes of satellites are found around other large galaxies (Ibata et al. 2014a, 2015; Cautun et al. 2015a,b; Phillips et al. 2015). This is important to confirm since it will determine whether this is a generic property of satellite distributions, or if the Local Group is simply peculiar. Pawlowski, Kroupa & Jerjen (2013) have shown that there is evidence of a link between planes of galaxies and satellites within the Local Group.

Proposed theories to explain this contrived distribution include mergers between M31 and other galaxies (Sawa & Fujimoto 2005), which result in tidal dwarf galaxies that would form in a plane (Kroupa 1997; Gentile et al. 2007; Hammer et al. 2013, 2015). However, this appears unlikely in a cold dark matter framework due to the implied lack of cold dark matter in the tidal dwarfs, which strongly contradicts inferred dark matter abundances of the observed dwarf spheroidals (Mateo 1998; Walker et al. 2007; Strigari et al. 2008; Strigari, Frenk & White 2010).

Another suggestion has been that the satellite galaxies were accreted along filaments that feed the host galaxy (Libeskind et al. 2005, 2015; Zentner et al. 2005; Lovell et al. 2011; Wang, Frenk & Cooper 2013; Tempel et al. 2015). Although all satellites would have coherent motions, the probability of producing the highly ordered system of satellites found in the Local Group has been argued against by Pawlowski et al. (2012, 2014). It also offers no explanation for the apparently short duration these satellites have been accreted over. Other studies have suggested it would be difficult to produce the satellite galaxies with low orbital angular momentum in this fashion (see e.g. Angus, Diaferio & Kroupa 2011).

Another prospect is for a group of galaxies to be accreted (D'Onghia & Lake 2008; Li & Helmi 2008). This would have the interesting property of ensuring that the satellite galaxy distribution was relatively compact and has the potential to produce low-angular momentum galaxies during the encounter between the host and the group. This idea was argued against by Metz et al. (2009) on the basis that in the study of Tully et al. (2006), there are no observed galaxy associations that are as thin as the MW's disc of satellites. Although it is true that the rms-projected radii of the galaxy associations identified by Tully et al. (2006) (∼150 kpc) are far larger than the thickness of the MW's disc of satellites, that does not rule out the possibility that a component of a galaxy group is more compact. In fact, the majority of the brightest galaxies in each group have a very nearby companion of much lower luminosity, as we demonstrate later. Moreover, the pertinent observation is whether the tight groups proposed by D'Onghia & Lake (2008) exist at moderate redshifts. It is conceivable that a high fraction of all tight groups have been tidally destroyed by redshift zero. This group infall scenario has regained popularity recently with several studies pointing out the possibility that a reasonable fraction of the Local Group's satellites originally formed in groups (Deason et al. 2015; Wetzel, Deason & Garrison-Kimmel 2015; Wheeler et al. 2015; Yozin & Bekki 2015; Smith et al. 2016).

A further peculiarity with regards to the satellite system of Andromeda is that the satellites that are part of the corotating thin plane are consistent with lying only in an arch surrounding M31, they very possibly do not encircle it. Thus, it makes sense to investigate scenarios where the satellites would intrinsically lie in such a distribution. In any case where the satellites fall from a large distance, they will execute a parabolic orbit. Depending on the impact parameter and the mass of Andromeda, this could result in satellites observed mostly in an arch around M31. This scenario has to satisfy the 3D positions of the satellites relative to M31 and their line-of-sight velocity.

Here we investigate the likelihood of a variant on the group infall scenario, such that, instead of a large group centred on an M33 or Large Magellanic Cloud (LMC) size host (Deason et al. 2015; Wetzel et al. 2015; Sales et al. 2016), a subhalo of Andromeda along with all of its sub-subhaloes form significant quantities of stars and they execute a fly-by orbit that brings them close to M31. During the close encounter, the satellites are strewn out around M31. Using *N*-body simulations, we explore the probability that these sub-subhaloes now represent the majority of the corotating satellites of Andromeda that lie in a thin arch. An idea somewhat similar to this one was simultaneously considered by Smith et al. (2016) who concentrated on a 1:2 mass ratio encounter between two MW/M31 mass galaxies and the survivability of such a corotating plane of satellites, but did not concentrate on the likelihood of their scenario reproducing the observed positions and velocities of the observed satellites. Here we explicitly focus on a statistical analysis of our scenario matching the detailed observed properties of M31's VTC plane of satellites.

In Section 2, we introduce the subhalo scenario and the simulation setup, in Section 3, we discuss the satellite sample and their re-orientation to facilitate comparison with the simulations. In Section 4, we present our statistical comparison of the sub-subhalo distribution with the observed satellite distribution of Andromeda and in Section 5, we discuss the results and draw our conclusions.

2 THE SUBHALO SCENARIO

Our ansatz is that due to photoionization effects (see e.g. Efstathiou 1992; Bullock, Kravtsov & Weinberg 2000; Benson et al. 2002; Dijkstra et al. 2004; Slater & Bell 2013; Wetzel et al. 2013;
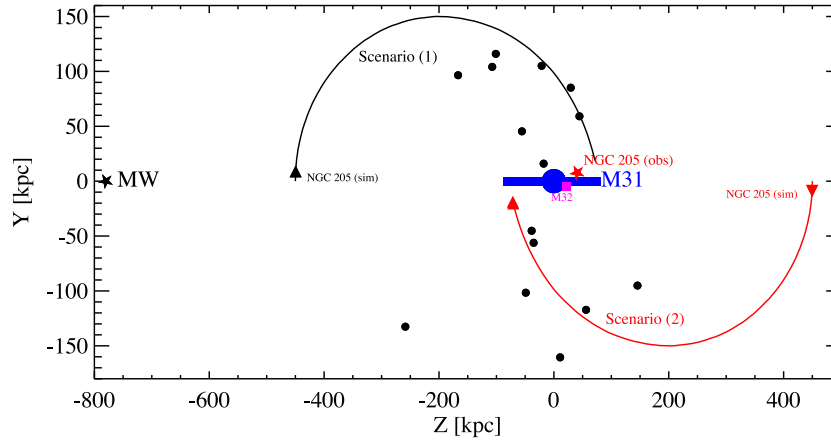
Figure 1. The positions of the large galaxies (the Milky Way, M31, M32 and NGC 205) and observed satellites (black circles) in the plane of the proposed orbit of NGC 205 around M31. We show the orbital paths of the two scenarios (1 with a black line and 2 with a red line). The Z-coordinates for NGC 205 and M32 are the maximum likelihood values from McConnachie et al. (2005), but their errors may be as high as $\sim$70 kpc (see Section 2.1.1 and de Grijs & Bono 2014).

Boylan-Kolchin, Bullock & Garrison-Kimmel 2014), only the latest accreted subhaloes had substantial numbers of bright sub-subhalo companions. Any subhaloes accreted earlier would have suffered from the bright UV halo originating from M31, stifling the formation of stars in their sub-subhaloes. This would require a sort of patchy re-ionization, perhaps the kind suggested by Castellano et al. (2016) or Sharma et al. (2016). Any subhalo that weighed more than a few per cent of the host would similarly quench their own sub-subhaloes, and any subhalo weighing much less than 1 per cent of the host would not have a significant, observable sub-subhalo distribution. In principle, this could leave a reasonably small window of subhalo masses with accompanying, bright sub-subhaloes.

The advantage of an accreted subhalo over a generic group is that the sub-subhalo mass function might closely reflect that of the observed satellites in the VTC plane (see Section 3.2). Furthermore, the mass of the subhalo might reflect the mass of a larger satellite at the centre of the observed satellite distribution. A corollary of this is that a significant fraction of galactic satellites could originate from subhalo groups on long-period orbits.

In our scenario, NGC 205 (M110) was the brightest galaxy of one of M31's largest subhaloes. Thus, the stellar component of NGC 205 sat at the centre of the subhalo. This subhalo was surrounded by hundreds of sub-subhaloes, of which only a fraction (the most massive) produced large quantities of stars. It is our assertion that after a close pericentric passage of M31, the sub-subhaloes were spread out along the orbital direction, but tidally compressed in the direction transverse to the orbit. If this effect is strong enough, under certain conditions, then this could, in principle, explain the VTC plane of satellites surrounding M31 (Ibata et al. 2013).

2.1 The simulation coordinate system

To visualize the geometry of the scenario, we have plotted two orthogonal views. The first, shown in Fig. 1, is the y-axis versus the z-axis, which is the orbital plane that NGC 205 moves in. The z-axis is set by the line between the MW (Y, Z) = (0–783 kpc) and M31 (Y, Z) = (0 kpc, 0 kpc). The y-axis is simply the height above or below M31. We test two different scenarios. The first, which we call scenario 1, is that NGC 205 began several Gyr ago from a position between M31 and the MW. It initially moved in the positive Y-direction and finally ended now just behind M31 moving in the

negative Y-direction. Alternatively, we could have scenario 2 where NGC 205 initially sits several hundred kpc behind M31 and orbits in the negative Y-direction. It orbits towards M31 and the MW and currently sits before M31, on the MW's side, and is moving in the positive Y-direction. The difference between the two scenarios is that (1) requires NGC 205 to sit just beyond M31 and (2) just in front of it.

2.1.1 Distance to NGC 205

One might suspect that the uncertainties on the distance to NGC 205 could easily allow both possibilities, however, according to McConnachie et al. (2005) the distance to NGC 205 using the tip of the red giant branch (TRGB) method is $d_{\mathrm{NGC205}} = 824 \pm 27$ kpc. Using a distance to M31 of $d_{\mathrm{M31}} = 783$ kpc, this gives a separation of around 41 kpc and thus a 1σ range of roughly 14–68 kpc (meaning NGC 205 is behind M31). Alternatively, de Grijs & Bono (2014) give recommended values in their review of distances to Andromeda galaxies with larger errors. From their table 4, the 1σ range for the separation between M31 and NGC 205 using the TRGB is given as -67 to 75 kpc, thus allowing NGC 205 to be in front of or behind M31. We thus consider both scenarios.

The majority of the satellite galaxies with Y-coordinate greater than 0 (or above M31 and NGC 205) are moving with a line-of-sight velocity away from the MW and those with a negative Y-coordinate (below M31 and NGC 205) are mostly moving towards the MW.

The second view, Fig. 2, is from the MW towards M31, showing us the plane of the sky. Here we see the recent orbit of NGC 205 through the thin plane of satellites which has a thickness which is surprisingly small in the X-direction.

We consider NGC 205 and not M32 because the former's lower velocity relative to M31 makes it a better candidate. Recent observations and theoretical models of M32 suggest it is actually on the MW's side of M31 (Jensen et al. 2003; Karachentsev et al. 2004; Dierickx, Blecha & Loeb 2014), but again this distance estimate is likely as uncertain as that of NGC 205.

2.2 Mass models for M31 and NGC 205

To simulate this scenario, we make N-body realizations for M31, NGC 205 and its dark matter subhaloes. M31 and NGC 205 are
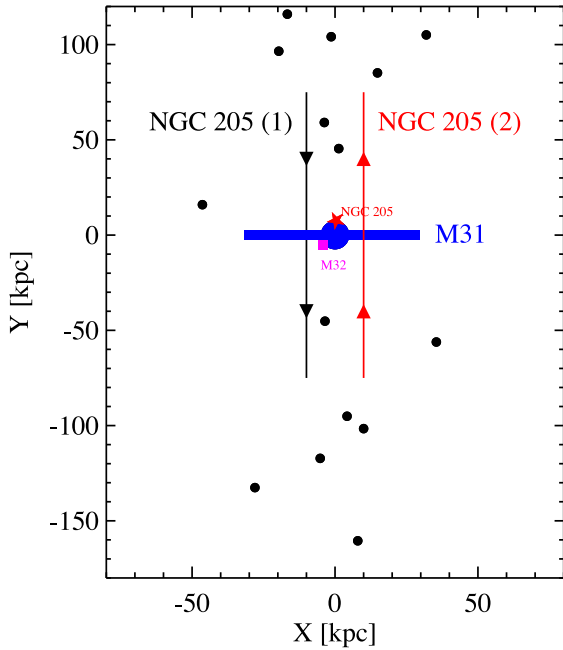
Figure 2. The positions of the large galaxies (M31, M32 and NGC 205) and observed satellites (black circles) in the plane of the sky. The Milky Way is located at $Z = -783$ kpc (out of the screen). We show the orbital paths of the two scenarios near pericentre (1 with a black line and 2 with a red line).

modelled with four components each: exponential stellar and gaseous discs, a Sérsic bulge (Graham & Driver 2005) and an NFW dark matter halo (Navarro, Frenk & White 1997).

We preface this by saying, besides the fairly well-constrained dark halo mass of M31, the only particularly important parameters are the extent of NGC 205's distribution of sub-subhaloes, and its dark halo mass. The baryonic parameters and the details of the dark matter distribution have very little influence on the outcome, but are included to add more realism to the simulations. In Table 1 and the following discussion, we describe the reference parameters for the mass models. It is to these values that variations, and references, are made in the remainder of the article.

2.2.1 M31

The M31 parameters were chosen to reflect the measured rotation curve from Kent (1989) and Widrow & Dubinski (2005) (but see also Carignan et al. 2006; Corbelli et al. 2010; Tamm et al. 2012). We use slightly tuned versions of the parameters used by Dierickx et al. (2014), in particular a Sérsic bulge (as opposed to a Hernquist bulge; Hernquist 1990; Baes & Dejonghe 2002) with a larger mass to better fit the inner rotation curve. The total dark halo mass of $M_{200} = 1.78 \times 10^{12}$ M$_\odot$ exceeds that found by the other analyses. One reason for this is that we do not consider globular clusters or

satellites good tracers of the galactic potential, for reasons evident from this article.

2.2.2 NGC 205

The NGC 205 parameters had relatively more freedom since its dynamics are less precisely constrained. Since it has likely suffered from the tidal influence of M31 during the orbit, matching the detailed dynamics using modelling like De Rijcke et al. (2006) or Geha et al. (2006) seemed beyond the scope of our paper. The parameters for NGC 205's dark matter halo are simply chosen to give it ~1 per cent the mass of M31's dark matter halo, i.e 1.8×10^{10} M$_\odot$, to ensure that the stellar component of NGC 205 occupies one of M31's largest subhaloes (Springel et al. 2008). Of course, there is no strict requirement for NGC 205 to occupy the most massive subhalo, so this remains a parameter with a substantial amount of uncertainty.

The radial distribution of the dark matter halo is chosen to give it a similar extent to the most massive subhaloes of the Aquarius project, thus it is similar to the dark halo profile of M32 from Dierickx et al. (2014) – which is a comparable dwarf galaxy in terms of its luminosity. The two most massive subhaloes surrounding the $M_{200} \sim 1.8 \times 10^{12}$ M$_\odot$ host halo (the same as our dark matter halo mass for M31) in Springel et al. (2008) have $r_{250} = 56.7$ and 55.3 kpc, whereas Dierickx et al. (2014) chose $r_{200} = 67$ kpc. We use $r_{200} = 60$ kpc, but again, the extent of the dark matter halo is less relevant than its overall mass since the sub-subhaloes orbit at large distances.

For the baryonic components of NGC 205, nominal values were selected for broad agreement with the luminosity and size. According to McConnachie (2012), the *V*-band magnitude for NGC 205 is -16.5, which corresponds to a luminosity of $\sim 3 \times 10^8$ L$_\odot$. These luminosities can often be underestimated due to insufficiently modelled extinction or the difficulty to detect outer surface brightness profile (Crnojević et al. 2014), but we assume that these uncertainties are included in the unknown stellar mass-to-light ratio – which we set to $M/L_V \sim 2.7$ (e.g. Bell & de Jong 2001). Thus, the dark matter to baryonic (stars plus gas) mass ratio is 18.2, which is a reasonable value for such a galaxy and is just slightly higher than M31's value of 16.8.

The stellar mass of NGC 205 is split almost evenly between bulge and disc (as Dierickx et al. 2014 did for M32), even though it is a dwarf elliptical galaxy, since the galaxy might have changed morphology during the orbit. The exponential scaleheights of the stellar and gaseous discs are found from the scaling relation $h_z \approx 0.2 h_R^{0.633}$ (see Bershady et al. 2010; Angus et al. 2015).

2.2.3 Velocity distributions

The velocity distributions for all spherical components are sampled from their distribution functions. The distribution functions are found using potentials that assume a spherical gravitational field for the discs. The NFW haloes are generated using the truncation devised by Kazantzidis, Magorrian & Moore (2004) where we set

Table 1. Parameters for the reference *N*-body models of M31 and NGC 205. The effective surface density and radius for the bulge are Σ_e and R_e, respectively. The Sérsic index is n_s.

Parameter units	M_{DM} (10^{10} M$_\odot$)	ρ_s (10^6 M$_\odot$ kpc^{-3})	r_s (kpc)	r_{200} (kpc)	$M_\star$ (10^8 M$_\odot$)	$h_{R,\star}$ (kpc)	M_g (10^8 M$_\odot$)	$h_{R,g}$ (kpc)	M_b (10^8 M$_\odot$)	Σ_e (10^4 M$_\odot$ kpc^{-2})	R_e (kpc)	n_s
M31	178	15	15.4	185.0	600	5.9	80	5.9	377	12.5	1.93	1.71
NGC 205	1.8	1.1	8.38	60.0	4	0.5	2	0.5	3.9	380	0.1	4

$r_{dec} = r_{200}$. The discs themselves were initialized using the method of Hernquist ([1993]). The only difference is that an exponential vertical density distribution is assumed here in place of a $sech^2$ distribution.

2.2.4 Sub-subhalo distribution

The final component is the distribution of sub-subhaloes surrounding NGC 205. Note that we do not assume that the sub-subhaloes trace the dark matter distribution. Instead, we start with the Einasto number density distribution of subhaloes around their host found by the Aquarius project (Springel et al. [2008]), which goes like

$$n_{sub} \propto \exp\left(-\frac{2}{\alpha}\left[\left(\frac{r}{r_{-2}}\right)^{\alpha} - 1\right]\right). \quad (1)$$

Springel et al. ([2008]) do not report the distributions of sub-subhaloes, presumably because they are quite stochastic. However, they make it clear that the distribution of sub-subhaloes around their subhalo host is not expected to be exactly a scaled-down version of equation (1) because of tidal stripping and the fact the sub-subhaloes cannot easily be restocked, however, it is the most reasonable starting point. We previously set the virial radius of NGC 205 to $r_{200} = 60$ kpc. Per section 3.2 of Springel et al. ([2008]), we define the sub-subhalo distribution by setting $\alpha = 0.68$ and $r_{-2} = 0.81r_{200}$.

The influence of the parameter r_{-2}, as well as the masses of both galaxies' dark matter haloes and the orbital pericentre are investigated in the results section (see Section 4).

The sub-subhalo distribution extends well beyond the virial radius of NGC 205 (as far as 400 kpc). Although the actual number of massive sub-subhaloes (say $M_{sub\text{-}sub}/M_{sub} > 10^{-5}$) should only be of the order of 100, we simulate 200k in order to statistically compare with the observed satellites. Again, the velocity distribution is sampled from its distribution function, but the particles (each representing a sub-subhalo) are effectively massless.

2.3 Stability and simulation setup

To demonstrate the stability of the various components, we ran simulations of M31 in isolation and NGC 205 (with the orbiting sub-subhaloes) in isolation for 10 Gyr. Each galaxy was resolved with 10^6 particles and the particle masses were identical for each mass component. All simulations were carried out using the GADGET-2 *N*-body code (Springel [2005]). Plots showing the limited evolution of each mass component are given in the appendix (Figs [A1]–[A3]). Apart from some thickening of the disc components, the galaxies appear very stable. Of most relevance, the dark matter haloes are highly stable, as are the sub-subhaloes.

To test the hypothesis that the VTC plane of corotating satellites originates from a close tidal encounter between M31 and NGC 205, we need a simulation where such a close encounter occurs. To facilitate this, we give NGC 205 an initial offset of 450 kpc from M31 and a small tangential velocity. This means NGC 205 is initially at apocentre and will orbit towards a pericentre much closer to M31, as per Fig. [1]. A distance of 450 kpc was chosen to be sufficiently far away to give the tidal forces enough time to work on the sub-subhalo distribution, assuming that any further away the tidal forces would be minimal.

The range of initial tangential velocities we probe are between 25 and 80 km s^{-1}. In Diemand, Moore & Stadel ([2004]), they show (with the red circles in the bottom-right panel of their Fig. [3]) the 3D velocity dispersion of subhaloes as a function of radius normalized by the peak circular velocity of the dark matter halo (which here
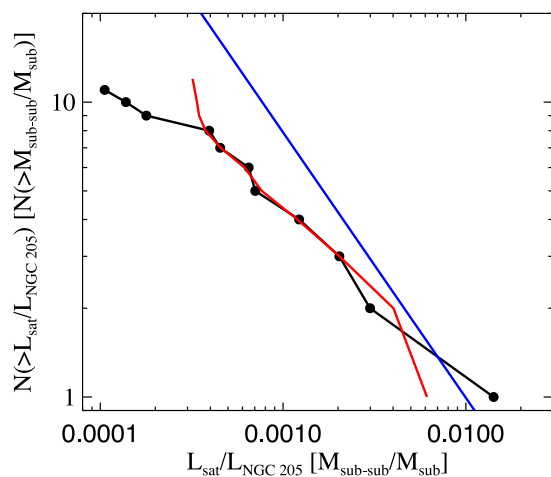

Figure 3. The filled black circles and connecting black line show the observed luminosity function of the satellite galaxies we propose originate from a subhalo group and now comprise the majority of the VTC plane of satellites. The red line is a simulated mass function of sub-subhaloes from a specifically selected subhalo group (Springel et al. [2008]). The blue line is the typical mass function of subhaloes around a host.

is around 200 km s^{-1}). Extrapolating this velocity dispersion to 2 virial radii should give the 3D velocity dispersion of a subhalo. Since the tangential motion is two out of three of these dimensions, it is reasonable to use the 3D velocity dispersion as an approximation. Thus, the expected tangential velocity dispersion for our initial conditions would be somewhere around 130 ± 30 km s^{-1}. Assuming a Gaussian distribution for the tangential velocities with the aforementioned tangential velocity dispersion and comparing with the cumulative distribution function, the fraction of orbits within the range of velocities we probe is thus around 0.31 and within a more conservative velocity range of 30–65 km s^{-1}, the fraction is around 0.2. Thus, the velocity ranges we consider are fairly typical of the expected velocities of subhaloes that are 2 virial radii from their host.

We also tested larger initial offsets and found no meaningful changes in the outcome. Ideally, this simulation should take place in a cosmological setting, but we assume here that the difference in orbital path and impact velocity are minor.

What is of relevance is not the initial offset, although this must be large enough to produce a suitable pericentric velocity, but rather the pericentre, or impact parameter. In order to affect different pericentric distances, or impact parameters, we simply vary the initial tangential velocity of NGC 205. Throughout the full orbit, but with greater cadence once NGC 205 is near pericentre, we compare the simulated positions and velocities of the sub-subhaloes with the observed satellites of M31.

3 COMPARING SIMULATED SUB-SUBHALOES WITH OBSERVED SATELLITES

3.1 Which satellite galaxies to include in the statistical sample

For the statistical comparison between the simulated sub-subhaloes and the satellites, one of the key questions is which satellite galaxies to include.

The satellite galaxies that Ibata et al. ([2013]) showed to be located in a vast, thin (but not exclusively corotating) plane around M31 are M32, NGC 147, 185, 205 and AND I, III, IX, XI, XII, XIII, XIV,

XVI, XVII, XXV, XXVI, XXVII and XXX (also known as C2). AND XXXII and LGS 3, which are catalogued by McConnachie (2012), are not included since they lie beyond the Pan Andromeda (PANDA) footprint where the vicinity is not fully surveyed. We do not include M32 since it is too massive to be part of the NGC 205 group. It is thus a shortcoming of our scenario and M32 would have to be an interloper. Alternatively, it could be bound to NGC 205 and co-orbiting with it like the two Magellanic Clouds. Or, it could be in a short period orbit of M31 given its small offset and line-of-sight velocity.

NGC 205 is obviously not included because it is a prior of the statistical calculation that it be close to the origin in the VTC plane. Four other satellites are handled on a case by case basis since, mainly for the line-of-sight velocity, they are less consistent than the others and we wish to gauge how significant their inclusion or exclusion is. AND XIII and AND XXVII do not share the same sense of rotation as the other satellites and are thus highly unlikely to be prior members of the subhalo group. Similarly, although AND XII and XXVI orbit with the correct orbital sense, their velocities appear somewhat less consistent with the scenario than the remaining 11.

On one hand, these counter-rotating satellites mean that our explanation for the thin disc of corotating satellites is incomplete. The alignment of AND XIII and XXVII with the plane of satellites would have to be coincidental. On the other, this would have to be the case for the majority of models attempting to explain the origin of the VTC plane of satellites, even modified gravity models creating tidal dwarf galaxies. Nevertheless, we still include them in our analysis of the likelihood of having so many satellites in a thin plane since even if they do not originate from a subhalo group centred on NGC 205, their coincidental alignment with the plane must be accounted for statistically.

Therefore, we have 13 satellite galaxies that are part of the VTC plane (including NGC 147, NGC 185, AND XII and AND XXVI); another 2 (AND XIII and AND XXVII) that are in the plane, but not corotating; M31 and NGC 205, which are expected to be there as the prior of the scenario; and M32 which is assumed to be in a short-period orbit of M31 and therefore neglected.

3.2 Subhalo group luminosity function

The advantage of using NGC 205 as the subhalo host of a distribution of sub-subhaloes is that we have a reasonable expectation of the mass function of sub-subhaloes. In fig. 19 of Springel et al. (2008), they show the cumulative mass function of sub-subhaloes within several subhaloes with each panel displaying a different subhalo. In Fig. 3, we show the observed cumulative luminosity function for the 11 satellite galaxies we assume comprised the subhalo group that became the VTC plane of satellites. This group excludes NGC 147 and 185 since they are too massive to be sub-subhaloes bound to NGC 205, as well as AND XIII and XXVII since they are counter-rotating. The former two satellites are often considered to be tidally bound to each other (however, see Evslin 2014), but are far too bright to have formed in the subhalo of NGC 205, i.e. to be associated with a sub-subhalo. The most logical explanation would be that they are each associated with another, less massive subhalo of M31 and became bound to NGC 205 during their orbit towards M31, similar to the LMC and the Small Magellanic Cloud (SMC) and NGC 147 and 185 themselves.

The luminosities for each galaxy are taken from the updated list of McConnachie (2012). Over the luminosity function of the observed satellite galaxies, we plot the simulated mass function of sub-subhaloes for a specifically chosen subhalo from Springel
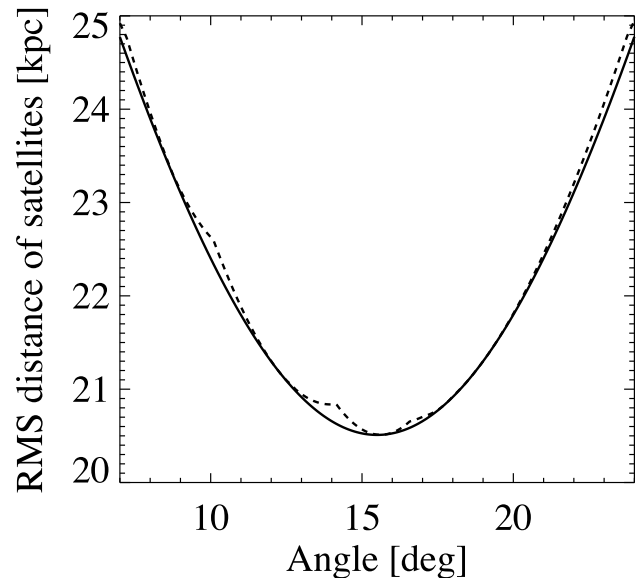

Figure 4. The rms distance of the 15 observed satellites in the VTC plane is plotted against rotation angle. The rms distances are computed relative to the mean *X* position of the observed satellites (solid line) and the median (dashed line).

et al. (2008), assuming that the ratio between satellite and host luminosity equals their dark matter halo mass ratios. This is the second subhalo group from their fig. 19 and it is given a red line as per the original plot. To a large extent, this simulated mass function resembles the observed luminosity function, thus we can say there is some evidence to suggest the luminosity function of the observed satellite galaxies is representative of the expected mass function of sub-subhaloes from simulations. We also overplot the standard mass function of subhaloes around a host galaxy (blue line), which can, of course, be determined with far greater precision.

3.3 Re-orienting the observed satellite galaxies for comparison

The observed distribution of satellite galaxies that belong to the corotating plane of satellites, as shown in fig. 1 of Ibata et al. (2013), is not exactly aligned with the vertical direction on the graph. Our simulations are set up such that NGC 205 and M31 are initially separated along the *Z*-direction and movement is exclusively in the *Y–Z* plane (see our Figs 1 and 2). Therefore, NGC 205 has no motion in the *X*-direction and our key comparison is between the *X*-distribution of the satellites and sub-subhaloes. To make comparison with the simulations easier, we simply rotate the observed satellites around the origin in the *X–Y* plane, which is chosen to be M31. In Fig. 4, we plot the rms distance of the 15 observed satellites from the *y*-axis as a function of rotation angle. We do this for two cases, one where the rms *X* distance is calculated relative to the mean *X* position of the satellites and another relative to the median. The rotation angle that minimizes the rms distance from the median *X* position of the observed satellites is 15°.6 and we rotate all satellites in the *X–Y* plane by this angle and subtract the median *X* value for all satellites.

To further align the observed satellites with the *Z–Y* plane of the simulations, we subtract 1.26 kpc from their *X*-coordinates. We do this to place the origin close to the centre of the VTC plane of satellites, but importantly mid-way between the two satellites with the smallest distance from the plane (i.e. smallest |*X*| values). This shift is important because if we place one satellite at

$X = 0$, it becomes meaningless to compute how many simulated sub-subhaloes have a smaller $|X|$-coordinate value.

This means that the observed NGC 205 sits at ($X_{NGC205} = 0.25$ kpc, $Y_{NGC205} = 7.7$ kpc) and half the satellites have larger Y values and half have lower. The observed M31 is at ($X_{M31} = -6$ kpc, $Y_{M31} = 0$ kpc) and the X-coordinate is the only one (including Y, Z and V_Z) for which M31 is not central. In the simulations, we ignore this subtlety and set $X = 0$ kpc for M31.

The extra constraint we have is that NGC 205 is currently moving with line-of-sight velocity relative to M31 of $V_Z = 54$ km s^{-1} and therefore the ideal instant to make any statistical comparison is when the simulated NGC 205 has its observed Y and V_Z values. Of course, this only happens once per orbit. Later when we refer to making comparisons near pericentre, we mean at this precise moment. When we wish to make a statistical comparison along the orbit, we will ignore the line-of-sight velocity whilst ensuring that the height of the simulated NGC 205 is very close to the observed 7.7 kpc.

3.4 Re-orienting the simulated sub-subhaloes for comparison and which regions to exclude

To compare the simulated sub-subhaloes with the observed satellites, we set the simulated M31 as the origin and we rotate NGC 205 and all its sub-subhaloes in the Z–Y plane until the Y-coordinates of the observed NGC 205, M31 and the MW (7.7, 0 and 0 kpc, respectively) are matched by the simulated ones. This allows us to compare the distribution of sub-subhaloes at any time, but the observed fact that NGC 205 is nearly in-line with M31 along the Z-direction is fixed. It also ensures that close to half of the sub-subhaloes are above NGC 205 (larger Y values) and half are below, as is observed.

Calculating any statistics from the distribution of sub-subhaloes requires some pre-filtering because the majority of the sub-subhaloes with low $|X|$ values have low Y values, i.e. the distribution is narrowest close to M31. However, no satellites are observed next to M31, in fact the closest satellites to M31 are beyond 40 kpc. Therefore, we assume that there are satellites close to M31, but they are just not detected. In order not to bias our statistics by considering sub-subhaloes in the region close to M31 where no satellites are found, we exclude all sub-subhaloes with $\sqrt{X^2 + Y^2} < 40$ kpc. We also exclude all sub-subhaloes with $Y > 135$ kpc and $Y < -180$ kpc, which are roughly the limits of the PANDAS footprint. These exclusion criteria are applied to all analyses, even if they do not directly concern the X-coordinate and we discuss their influence in Section 4.3.

3.5 Reference simulation

In Table 1, we list the reference set of parameters for our simulations. We refer to these parameters when listing the parameters of all other simulations. In the next section, we use scenario (2) from Figs 1 and 2 with an initial tangential velocity for NGC 205 of $V_Y = -60$ km s^{-1}, which in this case means a pericentre of $Z = -72$ kpc, to display some basic results and properties of the simulations.

For this reference simulation, we plot in Fig. 5 the on-sky projection of the observed M31 satellites, M31 and NGC 205. The simulated sub-subhaloes are plotted at the point near to pericentre when the simulation phase space coordinates of NGC 205 agree with the observed ones. The location of the observed M31 is shown by the blue galaxy, and only differs from the simulated position for the X-coordinate: in simulations $X_{M31} = 0$ kpc, whereas the observed M31 relative to the other satellites is $X_{M31} = -6$ kpc. The
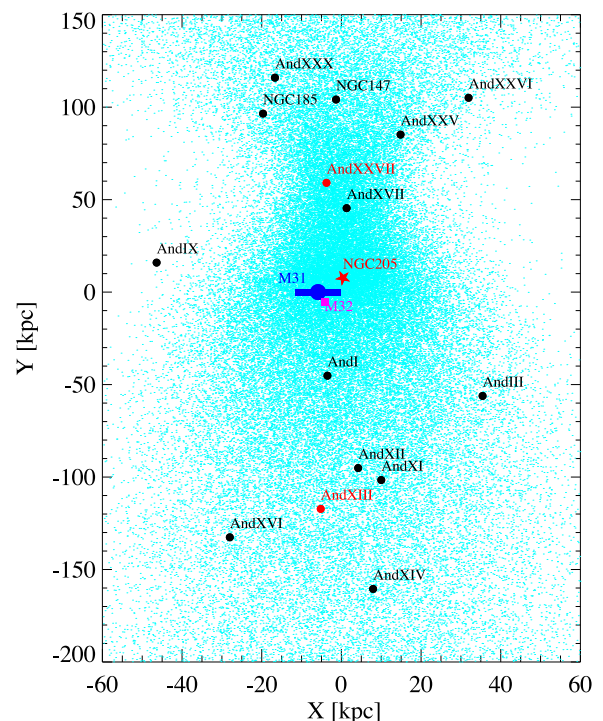

Figure 5. The sub-subhaloes and observed satellites in the X–Y plane (i.e. perpendicular distance from the VTC plane and plane of the sky location above or below M31) at the time when the observed and simulated coordinates for NGC 205 are identical. The 13 observed satellites that we propose originated from a subhalo group are represented by the black filled circles and their names are indicated. The turquoise dots signify the simulated sub-subhaloes. The red star is the location of the observed NGC 205 (identical to the simulated location). Although we plot the observed location of M31 with the blue galaxy shape, the simulated M31 is at the origin. M32 is located at the pink square, while AND XIII and XXVII are shown as red circles because they are not considered to have originated from the subhalo group.

simulated NGC 205 is identified by the red star and the only difference between simulated and observed coordinates is that the true line-of-sight distance Z_{NGC205} is more open to debate than the other coordinates (see Section 2.1.1).

This pericentric distribution of sub-subhaloes in Fig. 5 can be compared with the distribution at the beginning of the simulation before any tidal distortion (Fig. A4). Clearly, the close pericentric passage significantly narrows the sub-subhalo distribution in the X-direction and greatly extends it radially in the Y-direction.

4 RESULTS

In what follows, we discuss a series of statistical tests chosen to estimate the likelihood that the sub-subhalo scenario led to a thin plane of satellites, as well as the observations of the other phase space coordinates (Y, Z and V_Z).

4.1 Tests of the X-distribution/plane thickness

4.1.1 Kolmogorov–Smirnov test

We used a Kolmogorov–Smirnov (KS) test to compare the cumulative distributions of the observed satellites and simulated sub-subhaloes in the X-direction. These distributions are plotted for the reference simulation in Fig. 6 at the time when the simulated position of NGC 205 matches the observed Y and V_Z values (close to
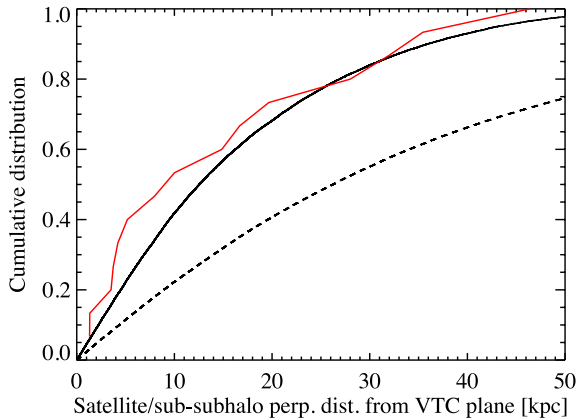
Figure 6. Cumulative distribution of distances, |X|, perpendicular to the VTC plane for our reference simulation. The solid red line includes all 15 observed satellites, including the counter-rotating AND XIII and XXVII, but excludes M32. The dashed black line is the simulated sub-subhalo cumulative distribution of the initial conditions. The solid black line uses the simulated positions of the sub-subhaloes at the time when the simulated coordinates of NGC 205 match the observed ones.

Figure 7. Cumulative distribution of distances, |X|, perpendicular to the VTC plane for our reference simulation. The solid red line represents the 15 observed satellites (including AND XIII and XXVII, but excluding M32). Each of the 1000 black lines represents the cumulative distribution of 15 randomly sampled simulated sub-subhaloes from a snapshot near pericentre. The green lines are sampled distributions of 15 sub-subhaloes that never cross the red line and are thus thinner than the observed satellite plane.

pericentre). The red line is the observed cumulative distribution of the 15 satellites (thus including AND XIII and AND XXVII, but excluding M32). Employing the aforementioned exclusion criteria for sub-subhaloes close to M31, we show the solid black line which is the simulated cumulative distribution for the reference parameters at the time corresponding to Fig. 5 – near pericentre. The dashed black line is the distribution at the beginning of the simulation (i.e. corresponding to Fig. A4). The maximum difference between the solid red and black cumulative distributions, which defines the KS-test statistic, is approximately 0.165. The KS-test statistic for the initial distribution of sub-subhaloes (dashed black line in Fig. 6) is ≈0.32, so clearly the tidal encounter efficiently redistributes them.

We can reject the null hypothesis that the original sub-subhalo distribution and the observed satellites come from the same parent distribution at >99.9 per cent confidence. At pericentre, the KS-test statistic is 0.17, but in order to reject the null hypothesis with merely 80 per cent confidence, it would have to be higher than 0.26.

4.1.2 Monte Carlo sampling technique

Given the distribution of the sub-subhaloes near pericentre, the frequency with which we would draw 15 sub-subhaloes (corresponding to the 13 corotating and 2 counter-rotating) with perpendicular distances from the VTC plane, |X|, that are lower than the 15 observed satellites can be estimated. For example, if we only had two observed satellites at 20 and 60 kpc, then a random draw would be successful as long as the |X| of at least one sub-subhalo was below 20 kpc and the other was below 60 kpc. In Fig. 7, an example of this is given where, over the top of the observed cumulative distribution (red line) of satellite distances, |X|, perpendicular to the VTC plane, we plot the cumulative distribution of 1000 randomly drawn sets of 15 sub-subhaloes from our reference simulation. A small fraction of these samples (which are given green lines) have thinner distributions than the observed satellites where the green line never crosses the red line. Sampling the simulated sub-subhalo distribution 500k times, we estimated that a distribution thinner than the observed one is found ∼1 per cent of the time for the reference simulation.
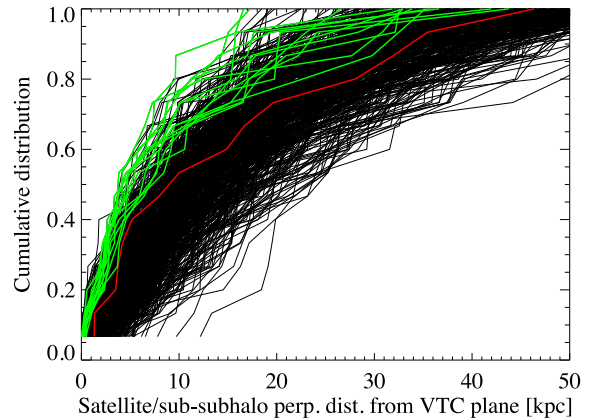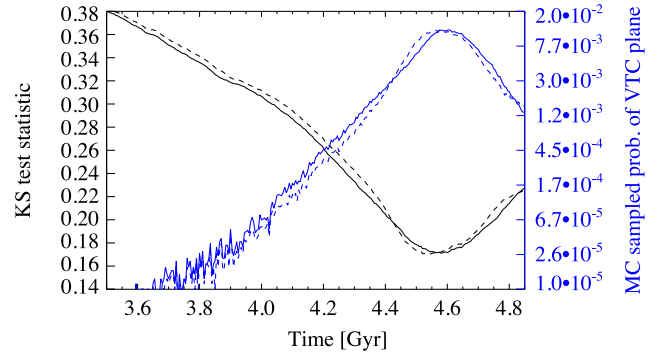

Figure 8. The black lines, which relate to the left-hand y-axis, are the Kolmogorov–Smirnov statistics comparing the simulated and observed distances, |X|, perpendicular to the VTC plane (i.e. the maximum difference between the solid black and red lines from Fig. 6) as a function of time for our reference simulation around pericentre. The blue lines correspond to the right-hand y-axis, which is log-scale, and are the Monte Carlo-sampled probabilities of producing a thinner distribution than the observed satellites from the instantaneous distribution of simulated sub-subhaloes. The solid lines refer to scenario 1 and the dashed lines to scenario 2.

As an aside, here we use NGC 205 as the dominant galaxy in the accreted subhalo, but in principle, M32 could be used instead. The probabilities of successfully reproducing the observations with M32 are typically an order of magnitude lower than with NGC 205.

In Section 4.5, we investigate the influence of tweaking various parameters on the derived probability.

4.1.3 Variation of probability/KS-test statistic along the orbit

In Fig. 8, we plot both the variation of the KS-test statistic and the Monte Carlo-sampled probability of sampling a thin distribution of sub-subhaloes, discussed in Sections 4.1.1 and 4.1.2, along the orbit for our reference simulation. The y-axis on the left-hand side displays the KS-test statistic and corresponds to the black lines. The logarithmic y-axis on the right-hand side displays the Monte Carlo-sampled probability and corresponds to the blue lines. Both
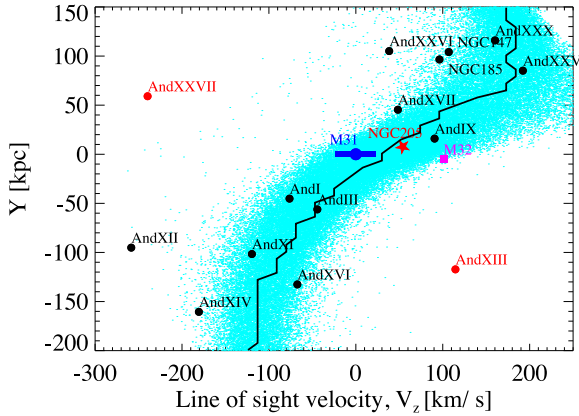
Figure 9. The sub-subhaloes and observed satellites in the V_Z–Y plane (i.e. line-of-sight velocity relative to M31 and plane of the sky location above or below M31) at the time when the simulated NGC 205's coordinates match the observed ones. The symbols are as per Fig. 5. A negative velocity means the object is moving towards the Milky Way. The coordinates of the simulated and observed M31 are identical. The errors in velocity are typically a few km s^{-1} and thus are roughly the size of the symbols (McConnachie 2012). The continuous series of points (V_{z_p}, Y_p) discussed in Section A1 is given as the black line.
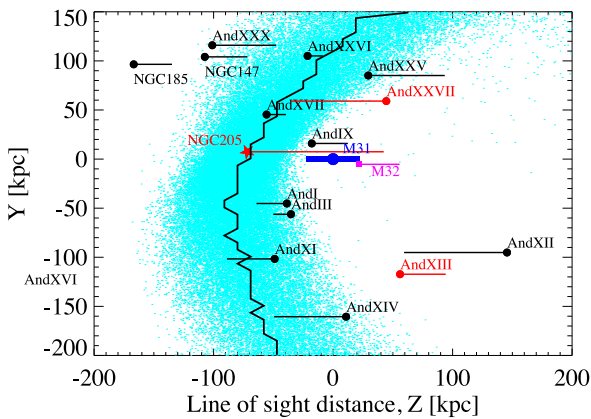

Figure 10. The sub-subhaloes and observed satellites in the Z–Y plane (i.e. line-of-sight distance and plane of the sky location above or below M31). The symbols are as per Fig. 5. The black line emerging from each data point represents the magnitude and direction of the satellite's line-of-sight velocity vector. The more positive the Z-position, the further away the object is from the Milky Way. The coordinates of the simulated and observed M31 are identical. The continuous series of points (Z_p, Y_p) discussed in Section A1 is given as the black line.

sets of lines display similar behaviour, as expected. When the KS-test statistic drops, the Monte Carlo-sampled probability increases. The KS-test statistic drops from 0.58 to 0.17 at pericentre and then quickly increases. The probability increases from 0 to 0.01 at pericentre. The probability stays above 0.005 for around 300 Myr.

4.2 General trends and coordinates of sub-subhaloes at pericentre

The distribution of distances, $|X|$, perpendicular to the VTC plane is not the only feature that must be reproduced, there is also the distribution of satellites in the Y-direction and the X–Y, Z–Y and V_Z–Y planes. The distributions of observed satellites and simulated sub-subhaloes are shown for the three planes in Figs 5, 9 and 10.

In Fig. 9, we plot the Y-positions of the observed satellites and simulated sub-subhaloes against their line-of-sight velocities, V_Z. The vast majority of the observed satellites overlap with the sub-subhaloes. The notable exceptions are of course the counter-rotating AND XIII and XXVII and this is precisely the reason they are not considered to be part of the VTC plane of satellites. Apart from those two, AND XII and XXVI are in regions of low probability and become increasingly more difficult to account for when using less extended initial distributions of sub-subhaloes.

In Fig. 10, we plot the Y-positions of the observed satellites and sub-subhaloes against their line-of-sight distances, Z, assuming scenario 2. Recall from Fig. 1 that using scenario 1 would lead to NGC 205 being located behind M31 with a positive Z. Each observed satellite has a line emerging from the data point, which indicates the direction and magnitude of its line-of-sight velocity vector. The line-of-sight distance for each satellite has a great deal more error associated with it than the line-of-sight velocity, so this is shown more for completeness than for a strict comparison. Clearly several observed satellites have substantial offsets from the turquoise band of simulated sub-subhaloes. In fact, AND XVI is not plotted because its coordinates $(Z, Y) = (-307\,\text{kpc}, -132\,\text{kpc})$ lie off the chart. Nevertheless, these offsets are typically less than 50 kpc, which is around 6 per cent at that distance ($\sim$780 kpc to M31). This is roughly the quoted accuracy of the TGRB distance measurement, although using Bayesian techniques, Conn et al. (2011, 2012) claim precisions as low as 2 per cent for the distances to some of the M31 satellites. The galaxies with larger than 50 kpc offsets are NGC 185, AND XII and XVI. Interestingly, AND XII is the same galaxy whose line-of-sight velocity is on the borderline of being too negative, but actually the quoted 1σ uncertainty on its distance is 136 kpc.

4.3 The concentration of sub-subhaloes in the Y-direction

We saw Fig. 5 previously and clearly the sub-subhaloes are not only narrow in the X-direction, but also highly extended in the Y-direction – as are the observed satellites. Having said that, the simulated sub-subhaloes in Fig. 5 do appear more concentrated in the Y-direction. In particular, we would expect to find more satellites near M31, but perhaps these are difficult to identify against the bright background of M31. Furthermore, the simulated sub-subhaloes decrease in density with increasing $|Y|$, but the observed satellites seem to be more prominent at larger $|Y|$. Clearly, the significance of these observations depends on the area around M31 that we mask and also the Y limits. In Section 3.4, we stated that we excluded all sub-subhaloes in an area $\sqrt{X^2 + Y^2} < 40\,\text{kpc}$ around M31, and below -180 kpc and above 135 kpc to exclude the region beyond the PANDAS footprint. However, the precise values of these limits can be argued, although the area around M31 cannot have a radius larger than 50 kpc or it would encroach upon AND I, IX and XVII. Similarly, $Y > -160$ kpc would exclude AND XIV, while $Y < 120$ kpc would exclude AND XXX.

To test the impact of these limits, we computed for the Y-direction an analogue to the probability of sampling a set of sub-subhaloes with a distribution that is thinner than the observed satellites in the X-direction. Since it appears difficult to produce as extended a distribution of sub-subhaloes in the Y-direction, we compute the probability that a sampled set of 15 sub-subhaloes is more extended in Y than the observed satellites. Thus, we consider a sample to be successful only if $|Y_{j,\text{ssh}}| > |Y_{j,\text{sat}}|$ for all $j = 1$–15. In Fig. 11, we plot the successful fraction of 500k random samplings for the Y-direction (dashed line) against two variables. The left-hand panel
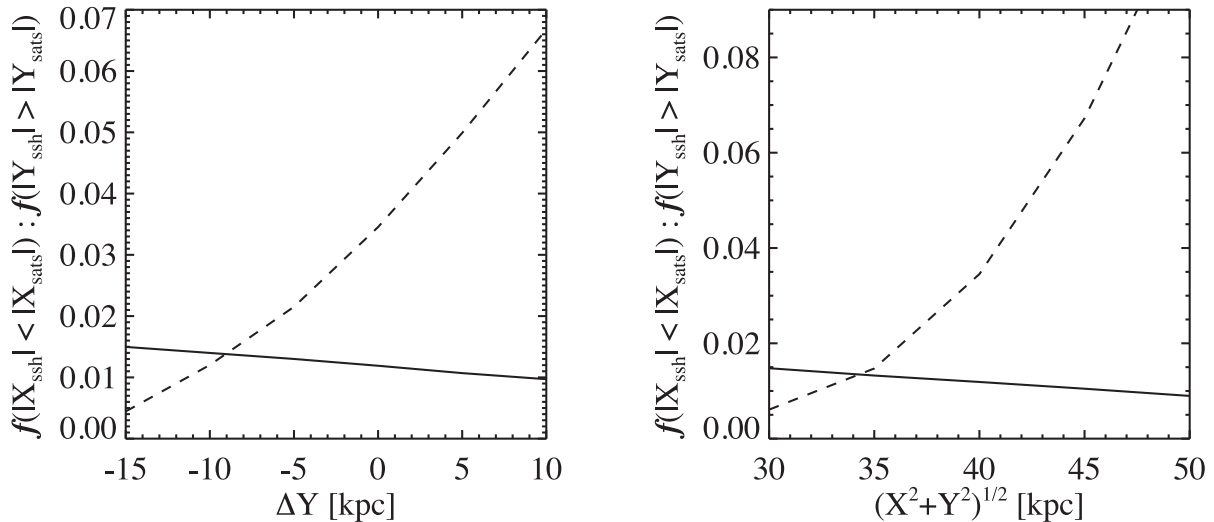
Figure 11. The Monte Carlo-sampled probability of producing as thin [extended] a distribution of simulated sub-subhaloes in the X (solid line) [Y (dashed line)]-direction as the observed distribution of satellites. We plot these quantities against two variables. In the left-hand panel, we vary the extent of the sampled distribution of sub-subhaloes from the default extent by the value on the *x*-axis. In the right-hand panel, we vary the radius of the centrally masked area surrounding M31, where the default radius is 40 kpc.

varies the upper and lower limits from -15 kpc to $+10$ kpc, meaning that for -15 kpc, we shorten the upper limit from 135 to 120 kpc and the lower limit we shorten from -180 to -165 kpc. We hold the radius of the masked region around M31 at the default 40 kpc. Unsurprisingly, the probability increases the broader we make the sampled area since the number of large Y sub-subhaloes increases. The black solid line shows how the probability of producing a thin distribution in the *X*-direction varies when the sampled area is extended. The influence is considerably weaker than in the *Y*-direction.

In the right-hand panel, we fix the upper and lower Y limits to the default values and vary the radius of the masked region around M31. Again, this has a strong influence on the probability of sampling an extended set of sub-subhaloes in Y, but a fairly weak influence on the chances of generating a thin distribution in X. To get a more constrained probability for the *Y*-direction, we would need to know conclusively that no satellites are present in the excluded regions. Until that time, the Y-distribution is a promising and likely fairly stringent, but unreliable gauge of the probability of our scenario replicating the observed distribution of satellites.

4.4 The concentration of sub-subhaloes in three dimensions

In Fig. 12, we plot the cumulative distribution of the 3D distances of the observed satellites (red line) from M31. We also plot the cumulative distribution of the 3D distances of the sub-subhaloes near pericentre from M31 (solid black line) and for the initial distribution (dashed black line). We use the standard exclusion criteria for the projected area around M31.

The KS statistic between the red and black solid lines is 0.2 meaning there is no evidence to suggest the two distributions are different.

4.5 Trends with parameter variations using a series of simulations

In addition to these plots of the KS-test statistic and the Monte Carlo-sampled probability of the thinness of the *X*-distribution (Fig. 8)
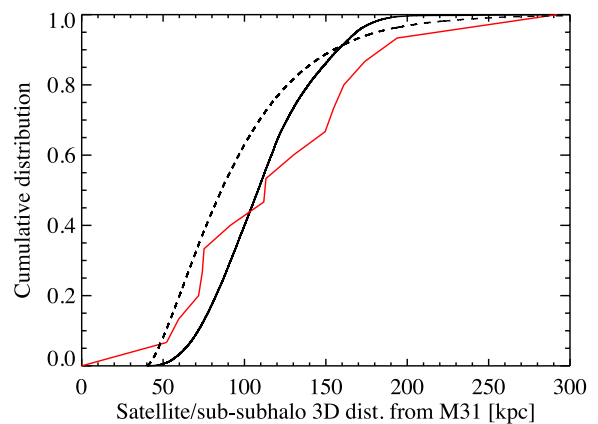

Figure 12. Cumulative distribution of the 3D distances of the observed satellites from M31 (red line). For comparison, we also show the cumulative distribution of the 3D distances for the simulated sub-subhaloes near pericentre (solid black line) and for the initial distribution of sub-subhaloes (dashed black line). The solid red line includes all 15 observed satellites, including the counter-rotating AND XIII and XXVII, but excludes M32.

with time near pericentre for the reference simulation, we also plot their values (and the probabilities for the extent of the Y-distribution) near pericentre for all our simulations in Fig. 13. The details of the different simulations are given in Table 2.

For ease of comparison, we separate the various simulations into blocks delineated by the vertical dashed turquoise lines. The first block is for simulations with the reference parameters (Table 1) but different initial tangential velocities (i.e. pericentres). We tried seven different values: 19, 24.5, 31, 37, 52, 72 and 126 kpc (25, 30, 35, 40, 50, 60 and 80 km s^{-1}; simulations 1–7). For these simulations, the values for the mass of M31, NGC 205 and the scaling of the sub-subhaloes distribution were exactly as per the reference parameters in Table 1. The second and third blocks have constant initial tangential velocity of 30 km s^{-1} and use the reference parameters, except for varying (2) the mass of NGC205 (30, 100 and 150 per cent of the reference value; simulations 8–10, respectively) and (3) the mass of M31 (80, 100 and 150 per cent of the reference
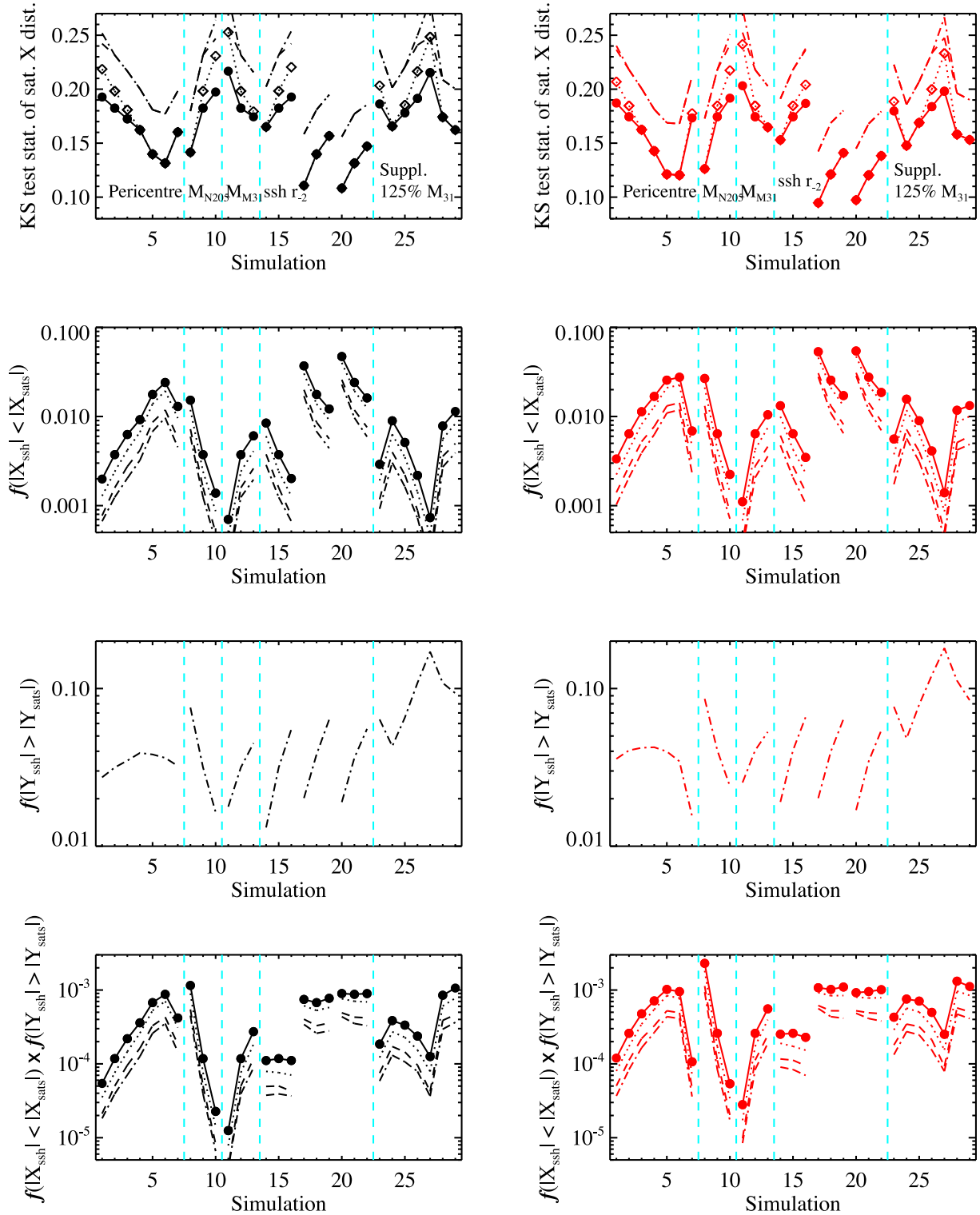
Figure 13. These figures show the variations in some parameters across our series of simulations listed in Table 2. The left-hand panel refers to scenario 1 and the right-hand panel to scenario 2 and this is the format for all four rows of figures. The top row shows the results of the KS test which was initially discussed in Section 4.1.1 and then discussed further in Section 4.5. The dot–dashed lines refer to all 15 satellites, the dashed lines exclude AND XIII, the dotted lines exclude AND XXVII and the solid lines (with filled circles) use neither of these two counter-rotating satellites. Using the same line types, the second row shows the Monte Carlo-sampled probability of producing a thinner distribution of sub-subhaloes in the *X*-direction than the observed satellite distribution as discussed in Section 4.1.2. The third row shows the Monte Carlo sampled probability of producing as extended a distribution of sub-subhaloes in the *Y*-direction as the observed distribution of satellites, as discussed in Section 4.3. For this, we only plot the dot–dashed line representing all 15 satellites. In the last row, we show the product of the Monte Carlo-sampled probabilities from rows two and three. The turquoise lines isolate related simulations to show the influence of (typically) a single parameter.

Table 2. Designations and parameters for the series of simulations. The second column gives the number of the simulation which corresponds to the *x*-axis values in Figs 13–15 and Fig. A7. The third column gives the initial tangential velocity and the following three columns are the scalings of the dark matter halo masses of NGC 205 and M31 and the radial scaling of the sub-subhalo distribution relative to the reference parameters from Table 1. A value of 100 per cent means the parameter is identical to the reference parameter.

Simulation	Number	V_Y (km s^{-1})	$M_{\rm NGC205}$ (%)	$M_{\rm M31}$ (%)	r_{-2} (%)
sim25	1	25	100	100	100
sim30	2	30	100	100	100
sim35	3	35	100	100	100
sim40	4	40	100	100	100
sim50	5	50	100	100	100
sim60	6	60	100	100	100
sim80	7	80	100	100	100
sim30m03	8	30	30	100	100
sim30	9	30	100	100	100
sim30m15	10	30	150	100	100
sim30a08	11	30	100	80	100
sim30	12	30	100	100	100
sim30a15	13	30	100	150	100
sim30r08	14	30	100	100	80
sim30	15	30	100	100	100
sim30r12	16	30	100	100	120
sim50r08	17	50	100	100	80
sim50	18	50	100	100	100
sim50r12	19	50	100	100	120
sim60r08	20	60	100	100	80
sim60	21	60	100	100	100
sim60r12	22	60	100	100	120
sim30a125r12	23	30	100	125	120
sim35a125r10	24	35	100	125	100
sim35a125r12	25	35	100	125	120
sim35a125r15	26	35	100	125	150
sim35a125r20	27	35	100	125	200
sim50a125r15	28	50	100	125	150
sim65a125r15	29	65	100	125	150

value; simulations 11–13 respectively). The fourth block varies only the radial scalings for the sub-subhalo distribution, r_{-2}, from 80, 100 and 120 per cent of the reference value for three different initial velocities (30, 50 and 60 km s^{-1} – simulations 14–16, 17–19 and 20–22, respectively). The last block is for simulations where the mass of M31 is always scaled to 125 per cent of the reference value. Amongst them, simulations 24–27 use a fixed initial tangential velocity of 35 km s^{-1} (pericentre of 27.5 kpc) and then scalings for the sub-subhaloes distribution of 100 per cent, 120 per cent, 150 per cent and 200 per cent. Scenario 23 has an initial tangential velocity of 30 km s^{-1} (corresponding to a pericentre of 22.5 kpc) and a sub-subhalo distribution inflated to 120 per cent of the reference value. Scenarios 28 and 29 use initial tangential velocities of 50 and 65 km s^{-1} (corresponding to pericentres of 46.5 and 72 kpc, respectively) and sub-subhalo distributions inflated to 150 per cent of the original.

For the KS-test statistic of the *X*-distribution in the first row of Fig. 13, and all subsequent rows of figures, we make separate plots for scenarios 1 and 2 (left- and right-hand panels, respectively). Scenario 1 is always plotted in black and scenario 2 in red. The different line types distinguish between the different number of observed satellites that we considered. The dot–dashed line considers all 15 satellites, the dashed line excludes AND XIII, the dotted line excludes AND XXVII and the solid line excludes both AND XIII and AND XXVII (which are the two counter-rotating satellites). Scenario 2 gives slightly lower KS-test statistics than scenario 1, but the trends with variables are the same: there is a

preference for lower NGC 205 masses, higher M31 masses and a tighter distribution of sub-subhaloes. The Monte Carlo sampling of the *X*-distribution of satellites, which is plotted in the second row of Fig. 13, exactly reflects the KS test – lower KS-test statistics lead to larger probabilities. The ideal initial tangential velocity, when using the reference mass for M31, appears to be around 60 km s^{-1} which gives a probability of 0.01. Regardless of the parameters we investigated here, the probability of creating such a thin distribution of satellites (ignoring the other dimensions) is at best a 1 in 30 chance.

The third row of Fig. 13 gives the probabilities of producing as extended a distribution of sub-subhaloes in the *Y*-direction as the observed satellites. Here we use the default exclusion limits as discussed in Sections 3.4 and 4.3. We only plot a single line-type corresponding to all 15 satellites since there is not a significant impact on the probability from the counter-rotating satellites. In the fourth row of Fig. 13, we give the product of the probability of producing a thin distribution in the *X*-direction and an extended distribution in the *Y*-direction (rows 2 and 3, respectively). Velocities around 50–60 km s^{-1}, low masses for NGC 205 and high masses for M31 are strongly preferred. Interestingly, the concentration of the sub-subhalo distribution does not appear to play a role.

4.6 Monte carlo sampling in more than one dimension

To compliment these illustrative probabilities, we made more concrete Monte Carlo samplings of the possibility that the
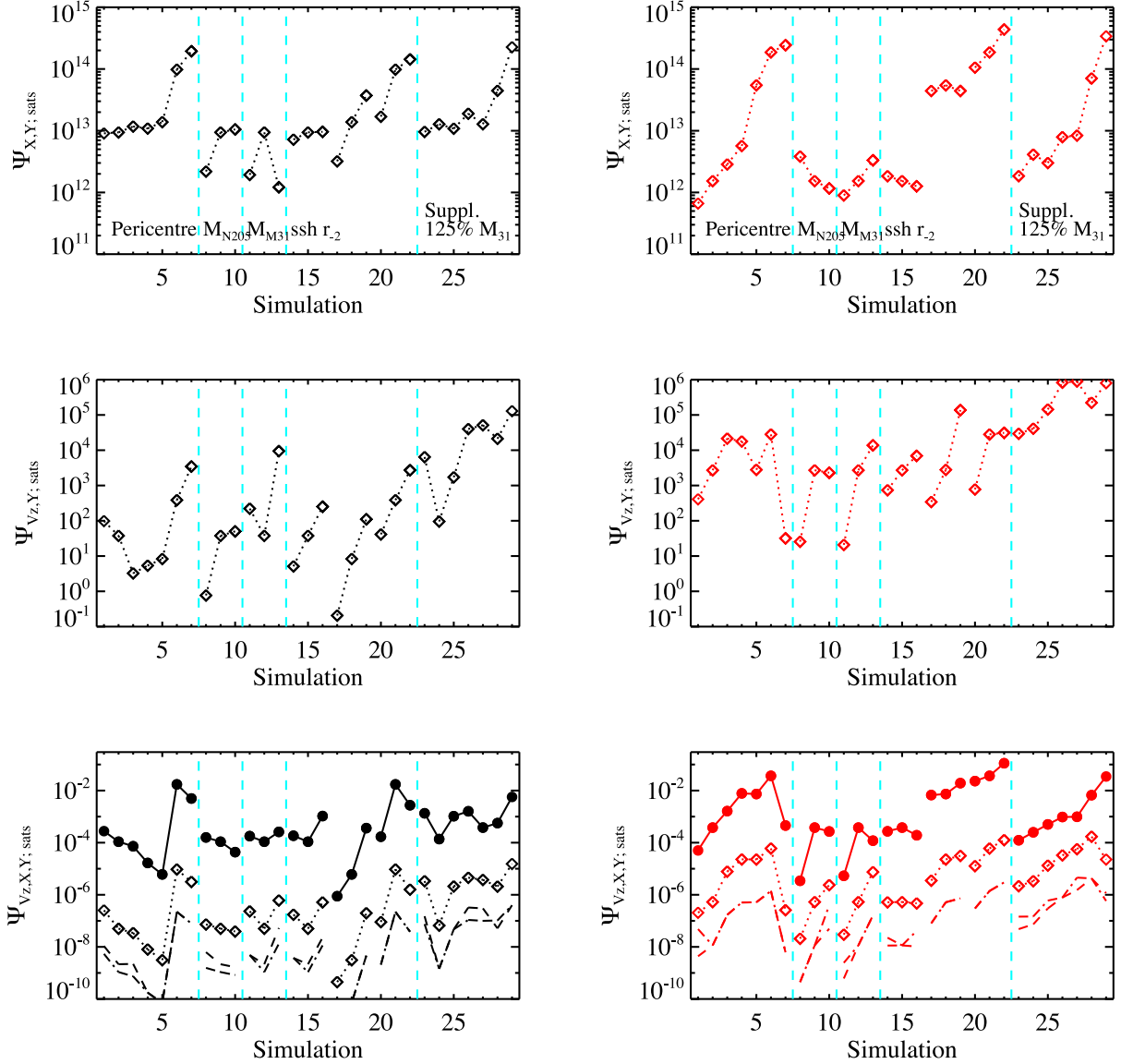
Figure 14. As per Fig. 13, these figures show the variations in some parameters across our series of simulations listed in Table 2. The left-hand panels refer to scenario 1 and the right-hand panels to scenario 2. The first and second rows show the variation in $\Psi_{X,Y;\text{sats}}$ and $\Psi_{V_Z,Y;\text{sats}}$, respectively, for the 13 corotating satellites as discussed in Section 4.6. The third row shows $\Psi_{V_Z,X,Y;\text{sats}}$ for the 11 core satellites (solid line with filled circles), the 13 corotating satellites (dotted line with empty diamonds), 14 satellites excluding AND XXVII (dashed) and 14 satellites excluding AND XIII (dot–dashed). The turquoise lines isolate related simulations to show the influence of (typically) a single parameter.

distribution of observed satellites comes from the sub-subhalo distribution near pericentre. We do this for the X–Y and V_Z–Y planes by initially calculating the number of sub-subhaloes within a small circle around each satellite in the plane divided by the total number of sub-subhaloes in the observed area (see Section 3.4 for a discussion of the excluded regions). For the X–Y distribution, this is simply the number within a radius of 10 kpc around the jth observed satellite and we refer to this as $n_j^{X,Y}$. For the V_Z–Y plane, we also use a 'radius' of $\lambda_{V_Z,Y} = 10\,\text{kpc}\,\text{km}\,\text{s}^{-1}$. We also do this for the 3D distribution X, Y and V_Z. We then take the product of each count separately over the selected number of satellites, such that $\Psi_{X,Y;\text{sats}} = \Pi_{j=1}^{N_{\text{sats}}} n_j^{X,Y}$, $\Psi_{V_Z,Y;\text{sats}} = \Pi_{j=1}^{N_{\text{sats}}} n_j^{V_Z,Y}$ and $\Psi_{V_Z,X,Y;\text{sats}} = \Pi_{j=1}^{N_{\text{sats}}} n_j^{V_Z,X,Y}$. In the three rows comprising Fig. 14, we plot, respectively, the values for $\Psi_{X,Y;\text{sats}}$, $\Psi_{V_Z,Y;\text{sats}}$ and $\Psi_{V_Z,X,Y;\text{sats}}$ for all simulations, with a constant, but arbitrary numerical scaling. For

$\Psi_{X,Y;\text{sats}}$ and $\Psi_{V_Z,Y;\text{sats}}$, we only plot the values for the 13 corotating satellites to avoid clutter. It is worth noting that the typical value one finds for sampling the 13 satellites from a typical subhalo distribution around an M31-sized galaxy is around 1000 for $\Psi_{V_Z,Y;\text{sats}}$ and 10^{-12} for $\Psi_{V_Z,X,Y;\text{sats}}$, whereas values $>10^4$ and $>10^{-5}$ are easily achievable for the sub-subhaloes at pericentre. This simply means the sub-subhalo scenario is intrinsically more likely.

For the bottom two rows of Fig. 14, there are large differences between scenario 1 and 2 for the preferred initial tangential velocity. The key tension with the preferred parameters for only producing a thin disc of satellites, is the scaling of the sub-subhalo distribution. This arises because the observed satellites are relatively spread out around the trajectory of the turquoise dots in Fig. 9 and therefore a few satellites can only be surrounded by a sizeable density of sub-subhaloes if the sub-subhaloes are spread out more.
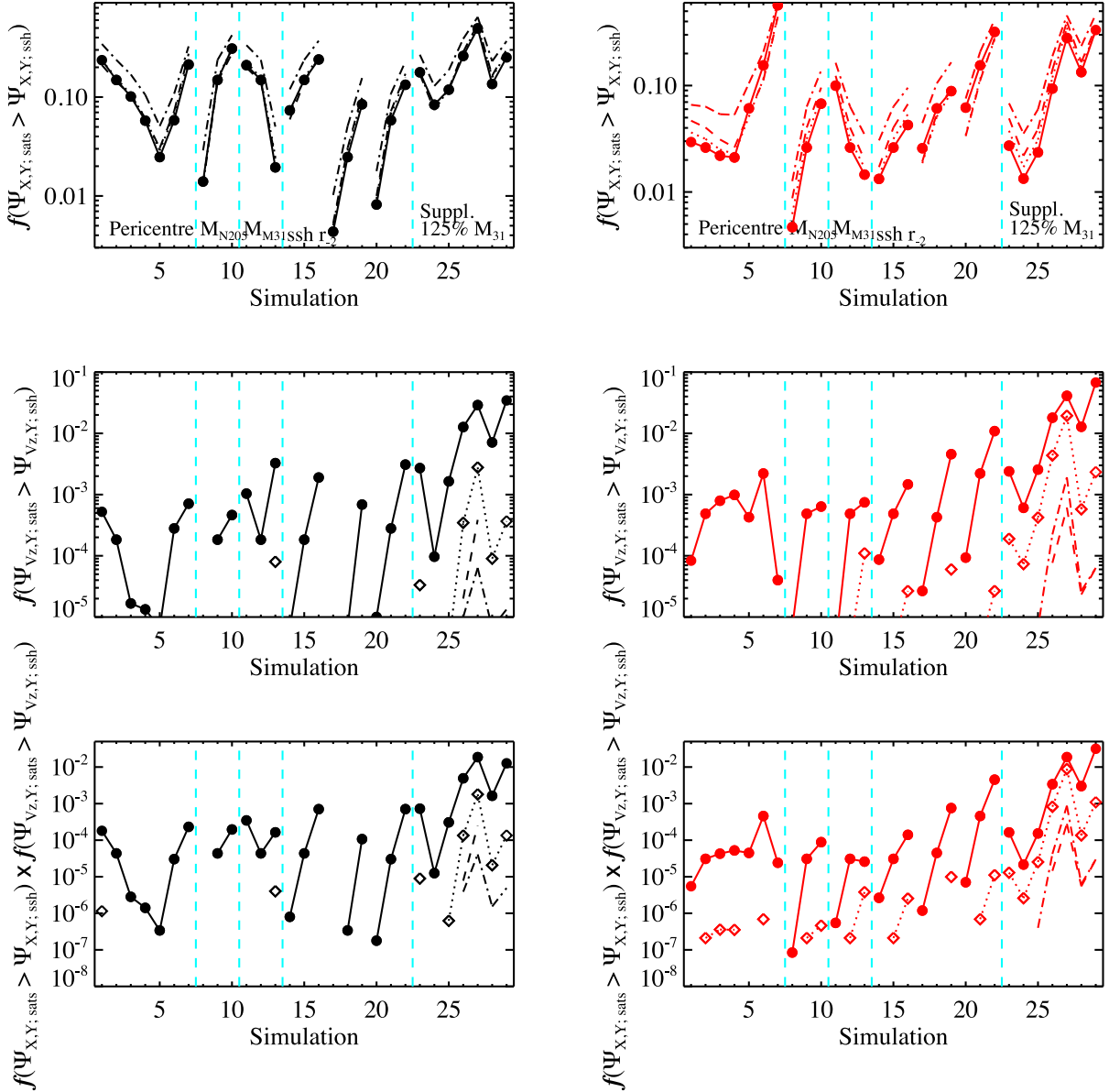
Figure 15. As per Fig. 13, these figures show the variations in some parameters across our series of simulations listed in Table 2. The left-hand panels refer to scenario 1 and the right-hand panels to scenario 2. The first and second rows show the Monte Carlo-sampled probability of producing the 2D distribution of satellites in the X–Y plane and V_Z–Y plane, respectively, as discussed in Section 4.6.1. The solid lines (with filled circles) represent the 11 core satellites, the dotted lines (with empty diamonds) represent the 13 corotating satellites, the dashed lines refer to 14 satellites excluding AND XXVII and the dot–dashed lines refer to 14 satellites excluding AND XIII. The final row shows the product of the probabilities from the top two rows. The turquoise lines isolate related simulations to show the influence of (typically) a single parameter.

4.6.1 Probabilities from Monte Carlo sampling in more than one dimension

We then repeated this analysis, but instead of calculating the number of sub-subhaloes around the selected number of observed satellites, we randomly selected the required number of satellites from the sub-subhalo distribution to represent the satellites. These statistical distributions we refer to as $\Psi_{X,Y;\mathrm{ssh}}$ and $\Psi_{V_Z,Y;\mathrm{ssh}}$, where ssh stands for sub-subhaloes. We do not use $\Psi_{V_Z,X,Y;\mathrm{ssh}}$ because there are insufficient sub-subhaloes to sample from, but for the other two, we compute 3×10^5 realizations with different random sets of sub-subhaloes representing the observed satellites. We quote the probability as the fraction of samplings for which $\Psi_{\mathrm{sats}} > \Psi_{\mathrm{ssh}}$

and we plot this for the X–Y plane and the V_Z–Y plane in Fig. 15. The dot–dashed lines include 14 satellites except for AND XIII, the dashed line only excludes AND XXVII and the dotted line excludes both counter-rotating satellites (AND XIII and AND XXVII). Although there is no reasonable justification for doing so, the solid line excludes both counter-rotating satellites and the two main outliers from the V_Z–Y satellite distribution (AND XII and AND XXVI).

The X–Y plane only weakly constrains the likelihood of the heights above the plane, but rather the 2D distribution of satellites in the plane of the sky. Here, the probabilities are not adversely affected by the counter-rotating satellites. The probability increases with higher NGC 205 masses, lower M31 masses and larger radial scalings of the sub-subhaloes distribution which is the exact

opposite of what was found for the *X* distribution. The trend of probability with initial tangential velocity changes from scenario 1 to 2, but velocities 50 km s^{-1} seem preferred for scenario 2.

For the V_Z–Y plane, the key difference is that a larger mass for M31 is favoured. There is not too much variation in probability with initial tangential velocity for scenario 2, although 60 km s^{-1} seems ideal. For scenario 1, velocities less than 60 km s^{-1} and greater than 30 km s^{-1} are disfavoured. It appears the most important parameter for this plane is simply the radial scaling of the sub-subhalo distribution: see simulations 24–27 where the scaling goes from 100 per cent to 200 per cent of the original size; and 14–16, 17–19 and 20–22 where it goes from 80 per cent to 120 per cent for three different initial tangential velocities. The main reason for this is that the spreading out of the sub-subhaloes allows the distribution to overlap with the dispersion of satellites in this plane which produces some moderate outliers (AND XII and AND XXVI). The probabilities for scenario 2 are generally slightly larger than scenario 1. A few simulations in scenario 1 have no measurable probability of even generating the 11 core satellites and very few simulations are able to match the observations well enough to have measurable probabilities when trying to account for 13 satellites. It seems this is only possible for larger masses of M31 and more extended sub-subhalo distributions. In fact, it seems like increasing the mass of M31 to 125 per cent of the reference mass for simulations 23–29 (and 150 per cent for simulation 13) is the key parameter for producing abetter match to all 13 corotating observed satellites. This follows because a larger mass for M31 leads to a larger tidally induced spread in sub-subhalo velocities.

An interesting result is that decreasing the radial extent of the sub-subhaloes and the mass of NGC 205 leads to increases in the probability of generating a very thin distribution of satellites, however, it also leads to dramatic decreases in the probability of reproducing the satellites in the V_Z–Y plane.

In the last row, we combine the two probabilities from the first two rows. This gives no consideration of the *Z*–*Y* positions, but the combination of measurement uncertainties for the line-of-sight distances and the general spread in the simulated sub-subhalo distribution should make this a relatively minor correction. These two panels in the last row show a clear preference for certain initial tangential velocities, with 60 km s^{-1} standing out for scenario 2. It also hints at a threshold mass for both M31 and NGC 205 below which the probability is negligible. Probably, the key factor is still the scaling of the sub-subhalo distribution with extended distributions preferred.

4.7 Unmodelled factors

The result of these probability studies is that despite the simulations broadly agreeing with the general patterns in the phase-space distribution of the satellites, the probabilities recovered suggest the situation is more intricate than our simple model. It is important to bear in mind that the scenario is generally plausible, meaning that it is possible to sample as thin a distribution of sub-subhaloes and the observed distribution of line-of-sight velocities and positions, but the resulting probabilities are low. We discuss below possible factors that may complicate the scenario.

The radial extent of the distribution of sub-subhaloes is not necessarily a simple scaled-down version of the subhalo distribution around M31 (or the MW). Tidal forces from M31 might truncate the sub-subhalo distribution at high redshifts and this more concentrated distribution would change the probabilities. Alternatively, our choice of r_{200} and also $r_{-2} = 0.81r_{200}$ might underestimate

the extent of the sub-subhalo distribution insofar as the probability of star formation in a sub-subhalo might be linked to that sub-subhalo's orbit. Probably, a more significant factor is just that the radial distribution of sub-subhaloes is stochastic and varies significantly from subhalo to subhalo and on top of that is anisotropic to some degree.

There is also the possibility that in-transit encounters have affected the distribution of sub-subhaloes. In particular, a scattering from M33 might have changed the orbit and also disturbed the sub-subhalo distribution meaning that a smooth distribution like we present here would struggle account for the resulting orbits. In the same vein, as mentioned in Section 3.2, the two larger satellites NGC 147 and NGC 185 are too massive to be members of the subhalo group of NGC 205. The most obvious reason for their proximity is that they became loosely bound to the group. In principle, their interaction with the group could also cause some minor variations in the velocities of the other satellites making them less ordered than our simulations suggest. In addition, M32's presence might have caused similar deviations from our predictions.

Another factor that has gained much attention recently is that any peculiarities in the Local Group, and deviations from expectations derived from simulations, might arise because the Local Group is composed of a pair of massive galaxies in close proximity. Many recent simulations like Garrison-Kimmel et al. (2014a) and McAlpine et al. (2016) make sure to focus only on areas of cosmological simulations with Local Group analogues when making comparisons between observations of the MW or M31 and simulated haloes. Several papers (for example Knebe et al. 2011; Fouquet et al. 2012; Teyssier, Johnston & Kuhlen 2012) look specifically at the exchange of satellites between M31 and the MW. There is clearly a continual interaction between these two galaxies. Nevertheless, this probably has little influence on the detailed probabilities of our scenario, but it could have important implications for the frequency of the interloping, counter-rotating satellites.

Most of these factors, in particular, the initial, anisotropic distribution of sub-subhaloes and the influence of in-transit encounters, would be automatically taken into account in cosmological simulations and that is clearly where more concrete answers must be sought.

4.7.1 Proper motions

The line-of-sight velocities of the simulated sub-subhaloes are relatively small for objects near pericentre that have orbited from a large distance. This is of course because the motion is mostly in the plane of the sky. For the initial velocities (pericentres) of 25, 30, 35, 40, 50, 60 and 80 km s^{-1} (19, 24.5, 31, 37, 52, 72 and 126 kpc), the motions in the plane of the sky at pericentre are roughly 530, 500, 460, 435, 390, 350 and 270 km s^{-1}, respectively. If measured, these large proper motions could provide a strong constraint on the scenario. Away from pericentre, these velocities would drop quickly meaning that the proper motions of the satellites, relative to M31, should decrease with *Y*-coordinate and NGC 205 should have the largest value. Such large orbital velocities are not unheard of in the Local Group. The Magellanic Clouds, in particular the LMC at >300 km s^{-1}, have very large tangential velocities relative to the MW (Kallivayalil et al. 2006a; Kallivayalil, van der Marel & Alcock 2006b; Piatek, Pryor & Olszewski 2007; Kallivayalil et al. 2013).

4.7.2 Galaxy associations

It has been argued that observed galaxy associations are too sparse or loose to explain the VTC plane of satellites. The absolute *V*-band magnitudes of NGC 205 and the brightest satellite in the corotating thin plane, AND I, are −16.5 and −11.9 – a difference of 4.6. Tully et al. (2006) presented the members of several galaxy associations that are independent of both each other and of Andromeda. NGC 3109 has a companion galaxy with *B*-band magnitude difference of 6.2 and projected distance of 25 kpc. According to Sand et al. (2015), it has a second dwarf companion at ∼72 kpc. Of the remaining four groups with satellites that are more than 3 mag dimmer than their host, three have companions with projected distances less than 45 kpc (32, 40.5 and 43.5 kpc) and magnitude differences between 5.1 and 7. One system does not have an observed nearby companion. Since these companion galaxies are typically at the observable threshold, it seems perfectly plausible that other, dimmer, nearby companions are present.

A common question is the location of these groups around M31 (or the MW), since others must have fallen in. The first point is there are only a handful of LMC/SMC- or NGC 205/M32-sized haloes expected from simulations. From the Aquarius project, there are five haloes more massive than $10^{10}\,\mathrm{M_\odot}$ and another seven more massive than $10^{9}\,\mathrm{M_\odot}$. Of those, the earlier accreted subhaloes might not have had a distribution of bright sub-subhaloes due to their proximity to M31. Furthermore, there is clearly not a bounty of SMC/NGC 205-sized haloes being accreted given that after the SMC and LMC, the MW has no massive nearby satellites.

Another related question, which we plan to investigate, is the survival of other discs of satellites. In particular, how long does it take to tidally destroy all satellites after infall?

5 DISCUSSION AND CONCLUSIONS

In this article, we explored the idea that Andromeda's vast, thin plane of corotating satellites is formed by the tidal break up of a subhalo group during a close pericentric passage of M31. NGC 205 was assumed to be the galaxy at the centre of the subhalo and it was initially surrounded by many bright sub-subhaloes. This is consistent with the observations of Tully et al. (2006) who found that the majority of independent nearby groups have a host and bright satellite (comparable to NGC 205 and AND I) within a projected distance of 25 and 45 kpc of each other. Deeper imaging is required to see if the dimmer satellites are present (Sand et al. 2015).

We showed that the observed luminosity function of the subhalo group, which we propose dispersed into the vast thin plane of satellites, is compatible with the mass function of sub-subhaloes from the simulations of Springel et al. (2008). Therefore, an advantage of this subhalo group scenario is that it could go some way to mitigating the TBTF problem, since only sub-subhaloes/satellites that are part of certain subhalo groups are lit up.

Using standard parameters, we made *N*-body models for M31, NGC 205 and 200 k point particles representing the sub-subhaloes which initially orbit NGC 205. NGC 205 and the sub-subhaloes initially began from a distance of around two times M31's virial radius and orbited towards M31 with a range of different velocities tangential to M31. The initial tangential velocity range was fairly typical of subhalo velocities from cosmological simulations. During the pericentric passage, the sub-subhaloes were spread out in the orbital direction, but they were compressed in the transverse

direction. This greatly improved the visual agreement with the observed distribution of satellites.

To compare the distribution of sub-subhaloes with that of the observed satellites in the *X*-direction (the distance perpendicular to the vast thin plane), we used a KS test and a Monte Carlo sampling method. For these tests, we used all 15 observed satellites including the 13 members of the VTC plane of satellites and the 2 counter-rotating satellites. We made all comparisons when the simulated location and line-of-sight velocity of NGC 205 agreed with the observed ones. Specifically, *X*, *Y* and V_Z were identical, but the line-of-sight distance *Z* from M31 depended on the initial tangential velocity.

We performed a series of simulations with different initial conditions facilitated by changing the initial tangential velocity (to give a different pericentre), the masses of NGC 205 or M31 and also the radial extent of the sub-subhalo distribution. The lowest KS-test statistics were found near pericentre, which NGC 205 is currently close to, and for the majority of our simulation parameter-space, the null hypothesis, that the sub-subhalo distribution and the observed satellites come from the same parent distribution, could not be rejected at any reasonable confidence level. The Monte Carlo sampling method to determine the probability of drawing a distribution of sub-subhaloes from our simulation that is thinner than the observed satellite plane gave a probability that varied significantly with the radial extent of the sub-subhaloes, the pericentre and the mass of NGC 205's dark matter halo. Using the reference distribution of sub-subhaloes and mass for NGC 205, we found the highest probability of producing a plane of satellites as thin as the observed 15 satellites was around 1 per cent.

Although the thin distribution of observed satellites in the *X*-direction is the most apparent concern, the highly extended distribution of observed satellites in the plane of the sky (*Y*-direction) is also troubling. To this end, we made a similar calculation of the probability of producing as extended a distribution satellites in the plane of the sky, but found that this depended critically on the size of the area that is excluded from sampling due to M31 saturating its surroundings and the chosen outer limits of the sampled region.

We also calculated the probability of agreement between the observed satellites and our simulations with Monte Carlo sampling of two combinations (1) the observed line-of+sight velocities with the *Y*-distribution, and (2) the *X*–*Y* plane (the plane of the sky). The *X*–*Y* easily gave probabilities greater than 0.1 for many sets of simulation parameters. The V_Z–*Y* plane showed very good visual agreement, bolstered by a self-devised quantity for the likelihood of the satellites relative to the simulated sub-subhaloes, discussed in Section A1. However, the details of the satellite phase-space distribution made a convincing match difficult. Ignoring the two counter-rotating satellites, the probability is still very low – at best around 10^{-4} unless the radial extent of the sub-subhaloes is inflated by 50 per cent or more. Such a tactic can increase the probability by a factor of 10 or more, but this in turn reduces the probability of randomly finding 15 satellites with very small distances perpendicular to the VTC plane. Ignoring two other marginal outliers (leaving 11 satellites) improves the best probabilities to 10^{-3} for the reference scaling of the sub-subhalo distribution and up to 10^{-2} for a mere 20 per cent increase in that parameter. If those two outliers must be included, then a slightly larger mass (at least 125 per cent of the reference value) for M31 is required. Although the probabilities we find for this scenario are seemingly low, they are still competitive with other models.

We argue that this may simply have to do with our model not being sophisticated enough to include potential encounters with other

galaxies along the orbit, such as M33, or simply M32, NGC 147 and NGC 185. Such encounters would inject a random component into the phase-space distribution of sub-subhaloes. Other complications might be that certain satellites are simply interlopers, or the initial sub-subhalo distribution is slightly anisotropic. Another factor that would increase the probability would be if there are as yet undiscovered satellites close to M31 within our excluded region of 40 kpc. We expect around 10 such undetected dwarf galaxies.

Thus, this scenario seems like an interesting candidate for explaining the bulk of the vast thin plane of corotating satellites and cannot yet be ruled out. There are still complexities that might be very important that are not accounted for here and really require high-spatial and temporal resolution cosmological simulations, such as the Caterpillar suite (Griffen et al. 2016) and Exploring the Local Volume in Simulations suite (Garrison-Kimmel et al. 2014a; McAlpine et al. 2016), the latter of which crucially focuses on binary Local Group analogues.

It will also be interesting to see how the scenario plays out for the MW satellite system, the detected plane of satellites around Centaurus A (Tully et al. 2015), as well as a second plane of satellites in Andromeda (Shaya & Tully 2013). To explain the second plane in Andromeda, there would need to be a separate encounter between a subhalo group of galaxies and M31. This implies that all low-mass satellite galaxies form in sub-subhaloes and their locations are caused by encounters with the host that separated them from their subhalo host.

To close, we re-emphasize the various assumptions on which this scenario rests, which are also predictions.

(i) Haloes like the MW, M31, LMC or M33 with $M_{\rm vir} > 10^{11}\,{\rm M}_\odot$ inhibit the star formation in their own nearby subhaloes, or tidally disrupt them.

(ii) Only subhaloes that fell from (or at least orbited to) well outside M31's virial radius formed large quantities of stars.

(iii) There is a subhalo mass window, $M_{\rm vir} \sim 10^{9\text{–}10}\,{\rm M}_\odot$, for which basically all bound sub-subhaloes formed significant numbers of stars.

(iv) The vast majority of galaxies with $M_{\rm vir} < 10^8\,{\rm M}_\odot$ do not form in isolation, but within the sub-subhaloes of a subhalo group.

(v) Every separate plane of satellites is caused by a distinct encounter between a subhalo group and a host galaxy.

(vi) M32, AND XIII and XXVII are interlopers of the VTC plane of satellites.

(vii) There should be around 10 undetected satellites within 40 kpc of M31.

(viii) NGC 147 and 185, which are gravitationally bound to each other, were also dragged by (or led) NGC 205 towards M31.

(ix) Field dwarf ellipticals with $M_{\rm vir} \sim 10^{9\text{–}10}\,{\rm M}_\odot$ should have observable dwarf satellites with the same luminosity function and spatial distribution as discussed here (following Springel et al. 2008).

(x) For reasonable parameters, and ignoring the other coordinates, the chance of producing as thin a distribution of satellites as the observed VTC plane at pericentre is less than roughly 1 per cent, therefore such ultrathin distributions should not be found around a statistically significant proportion of Andromeda-sized galaxies.

(xi) The proper motions of NGC 205 and the dwarf galaxies comprising the VTC plane of satellites should be large. For example, NGC 205 should have a plane of the sky motion of at least 300 km s^{-1} relative to M31. This was also predicted by Howley et al. (2008) to explain NGC 205's tidal features.

REFERENCES

Angus G. W., Diaferio A., Kroupa P., 2011, MNRAS, 416, 1401
Angus G. W., Gentile G., Swaters R., Famaey B., Diaferio A., McGaugh S. S., Heyden K. J. V. D., 2015, MNRAS, 451, 3551
Baes M., Dejonghe H., 2002, A&A, 393, 485
Bahl H., Baumgardt H., 2014, MNRAS, 438, 2916
Bell E. F., de Jong R. S., 2001, ApJ, 550, 212
Benson A. J., Frenk C. S., Lacey C. G., Baugh C. M., Cole S., 2002, MNRAS, 333, 177
Bershady M. A., Verheijen M. A. W., Westfall K. B., Andersen D. R., Swaters R. A., Martinsson T., 2010, ApJ, 716, 234
Boylan-Kolchin M., Bullock J. S., Kaplinghat M., 2011, MNRAS, 415, L40
Boylan-Kolchin M., Bullock J. S., Kaplinghat M., 2012, MNRAS, 422, 1203
Boylan-Kolchin M., Bullock J. S., Garrison-Kimmel S., 2014, MNRAS, 443, L44
Bullock J. S., Kravtsov A. V., Weinberg D. H., 2000, ApJ, 539, 517
Carignan C., Chemin L., Huchtmeier W. K., Lockman F. J., 2006, ApJ, 641, L109
Castellano M. et al., 2016, ApJ, 818, L3
Cautun M., Wang W., Frenk C. S., Sawala T., 2015a, MNRAS, 449, 2576
Cautun M., Bose S., Frenk C. S., Guo Q., Han J., Hellwing W. A., Sawala T., Wang W., 2015b, MNRAS, 452, 3838
Conn A. R. et al., 2011, ApJ, 740, 69
Conn A. R. et al., 2012, ApJ, 758, 11
Conn A. R. et al., 2013, ApJ, 766, 120
Corbelli E., Lorenzoni S., Walterbos R., Braun R., Thilker D., 2010, A&A, 511, A89
Crnojević D. et al., 2014, MNRAS, 445, 3862
D'Onghia E., Lake G., 2008, ApJ, 686, L61
Davis M., Efstathiou G., Frenk C. S., White S. D. M., 1985, ApJ, 292, 371
de Grijs R., Bono G., 2014, AJ, 148, 17
De Rijcke S., Prugniel P., Simien F., Dejonghe H., 2006, MNRAS, 369, 1321
Deason A. J., Wetzel A. R., Garrison-Kimmel S., Belokurov V., 2015, MNRAS, 453, 3568
Diemand J., Moore B., Stadel J., 2004, MNRAS, 352, 535
Diemand J., Kuhlen M., Madau P., 2007, ApJ, 657, 262
Dierickx M., Blecha L., Loeb A., 2014, ApJ, 788, L38
Dijkstra M., Haiman Z., Rees M. J., Weinberg D. H., 2004, ApJ, 601, 666
Efstathiou G., 1992, MNRAS, 256, 43P
Evslin J., 2014, MNRAS, 440, 1225
Fouquet S., Hammer F., Yang Y., Puech M., Flores H., 2012, MNRAS, 427, 1769
Frenk C. S., White S. D. M., Efstathiou G., Davis M., 1985, Nature, 317, 595
Frenk C. S., White S. D. M., Davis M., Efstathiou G., 1988, ApJ, 327, 507
Garrison-Kimmel S., Rocha M., Boylan-Kolchin M., Bullock J. S., Lally J., 2013, MNRAS, 433, 3539
Garrison-Kimmel S., Boylan-Kolchin M., Bullock J. S., Lee K., 2014a, MNRAS, 438, 2578
Garrison-Kimmel S., Boylan-Kolchin M., Bullock J. S., Kirby E. N., 2014b, MNRAS, 444, 222
Geha M., Guhathakurta P., Rich R. M., Cooper M. C., 2006, AJ, 131, 332
Gentile G., Famaey B., Combes F., Kroupa P., Zhao H. S., Tiret O., 2007, A&A, 472, L25
Graham A. W., Driver S. P., 2005, Publ. Astron. Soc. Aust., 22, 118
Griffen B. F., Ji A. P., Dooley G. A., Gómez F. A., Vogelsberger M., O'Shea B. W., Frebel A., 2016, ApJ, 818, 10

Hammer F., Yang Y., Fouquet S., Pawlowski M. S., Kroupa P., Puech M., Flores H., Wang J., 2013, MNRAS, 431, 3543

Hammer F., Yang Y. B., Flores H., Puech M., Fouquet S., 2015, ApJ, 813, 110

Hernquist L., 1990, ApJ, 356, 359

Hernquist L., 1993, ApJ, 86, 389

Howley K. M., Geha M., Guhathakurta P., Montgomery R. M., Laughlin G., Johnston K. V., 2008, ApJ, 683, 722

Ibata R. A. et al., 2013, Nature, 493, 62

Ibata N. G., Ibata R. A., Famaey B., Lewis G. F., 2014a, Nature, 511, 563

Ibata R. A., Ibata N. G., Lewis G. F., Martin N. F., Conn A., Elahi P., Arias V., Fernando N., 2014b, ApJ, 784, L6

Ibata R. A., Famaey B., Lewis G. F., Ibata N. G., Martin N., 2015, ApJ, 805, 67

Jensen J. B., Tonry J. L., Barris B. J., Thompson R. I., Liu M. C., Rieke M. J., Ajhar E. A., Blakeslee J. P., 2003, ApJ, 583, 712

Kallivayalil N., van der Marel R. P., Alcock C., Axelrod T., Cook K. H., Drake A. J., Geha M., 2006a, ApJ, 638, 772

Kallivayalil N., van der Marel R. P., Alcock C., 2006b, ApJ, 652, 1213

Kallivayalil N., van der Marel R. P., Besla G., Anderson J., Alcock C., 2013, ApJ, 764, 161

Karachentsev I. D., Karachentseva V. E., Huchtmeier W. K., Makarov D. I., 2004, AJ, 127, 2031

Kazantzidis S., Magorrian J., Moore B., 2004, ApJ, 601, 37

Kent S. M., 1989, PASP, 101, 489

Klypin A., Kravtsov A. V., Valenzuela O., Prada F., 1999, ApJ, 522, 82

Knebe A., Libeskind N. I., Knollmann S. R., Martinez-Vaquero L. A., Yepes G., Gottlöber S., Hoffman Y., 2011, MNRAS, 412, 529

Koch A., Grebel E. K., 2006, AJ, 131, 1405

Kroupa P., 1997, New Astron., 2, 139

Kroupa P. et al., 2010, A&A, 523, A32

Li Y., Helmi A., 2008, MNRAS, 385, 1365

Libeskind N. I., Frenk C. S., Cole S., Helly J. C., Jenkins A., Navarro J. F., Power C., 2005, MNRAS, 363, 146

Libeskind N. I., Hoffman Y., Tully R. B., Courtois H. M., Pomarède D., Gottlöber S., Steinmetz M., 2015, MNRAS, 452, 1052

Lovell M. R., Eke V. R., Frenk C. S., Jenkins A., 2011, MNRAS, 413, 3013

Lynden-Bell D., 1983, in Athanassoula E., ed., Proc. IAU Symp. 100, Internal Kinematics and Dynamics of Galaxies, Kluwer, Dordrecht, p. 89

McAlpine S. et al., 2016, Astron. Comput., 15, 72

McConnachie A. W., 2012, AJ, 144, 4

McConnachie A. W., Irwin M. J., Ferguson A. M. N., Ibata R. A., Lewis G. F., Tanvir N., 2005, MNRAS, 356, 979

Mateo M. L., 1998, ARA&A, 36, 435

Metz M., Kroupa P., Libeskind N. I., 2008, ApJ, 680, 287

Metz M., Kroupa P., Theis C., Hensler G., Jerjen H., 2009, ApJ, 697, 269

Moore B., Ghigna S., Governato F., Lake G., Quinn T., Stadel J., Tozzi P., 1999, ApJ, 524, L19

Navarro J. F., Frenk C. S., White S. D. M., 1997, ApJ, 490, 493

Pawlowski M. S., 2016, MNRAS, 456, 448

Pawlowski M. S., Kroupa P., Angus G., de Boer K. S., Famaey B., Hensler G., 2012, MNRAS, 424, 80

Pawlowski M. S., Kroupa P., Jerjen H., 2013, MNRAS, 435, 1928

Pawlowski M. S. et al., 2014, MNRAS, 442, 2362

Pawlowski M. S., McGaugh S. S., Jerjen H., 2015, MNRAS, 453, 1047

Phillips J. I., Cooper M. C., Bullock J. S., Boylan-Kolchin M., 2015, MNRAS, 453, 3839

Piatek S., Pryor C., Olszewski E. W., 2007, preprint (arXiv:0712.1764)

Planck Collaboration XVI, 2014, A&A, 571, A16

Sales L. V., Navarro J. F., Kallivayalil N., Frenk C. S., 2016, preprint (arXiv:1605.03574)

Sand D. J., Spekkens K., Crnojević D., Hargis J. R., Willman B., Strader J., Grillmair C. J., 2015, ApJ, 812, L13

Sawa T., Fujimoto M., 2005, PASJ, 57, 429

Sharma M., Theuns T., Frenk C., Bower R., Crain R., Schaller M., Schaye J., 2016, MNRAS, 458, L94

Shaya E. J., Tully R. B., 2013, MNRAS, 436, 2096

Slater C. T., Bell E. F., 2013, ApJ, 773, 17

Smith R., Duc P. A., Bournaud F., Yi S. K., 2016, ApJ, 818, 11

Spergel D. N., Bean R., Doré O., Nolta M. R., Bennett C. L., Dunkley J., Hinshaw G., Wright E. L., 2007, ApJ, 170, 377

Springel V., 2005, MNRAS, 364, 1105

Springel V. et al., 2008, MNRAS, 391, 1685

Strigari L. E., Bullock J. S., Kaplinghat M., Simon J. D., Geha M., Willman B., Walker M. G., 2008, Nature, 454, 1096

Strigari L. E., Frenk C. S., White S. D. M., 2010, MNRAS, 408, 2364

Tamm A., Tempel E., Tenjes P., Tihhonova O., Tuvikene T., 2012, A&A, 546, A4

Tempel E., Guo Q., Kipper R., Libeskind N. I., 2015, MNRAS, 450, 2727

Teyssier M., Johnston K. V., Kuhlen M., 2012, MNRAS, 426, 1808

Tully R. B. et al., 2006, AJ, 132, 729

Tully R. B., Libeskind N. I., Karachentsev I. D., Karachentseva V. E., Rizzi L., Shaya E. J., 2015, ApJ, 802, L25

Walker M. G., Loeb A., 2014, Contemp. Phys., 55, 198

Walker M. G., Mateo M., Olszewski E. W., Gnedin O. Y., Wang X., Sen B., Woodroofe M., 2007, ApJ, 667, L53

Wang J., Frenk C. S., Cooper A. P., 2013, MNRAS, 429, 1502

Wetzel A. R., Tinker J. L., Conroy C., van den Bosch F. C., 2013, MNRAS, 432, 336

Wetzel A. R., Deason A. J., Garrison-Kimmel S., 2015, ApJ, 807, 49

Wheeler C., Oñorbe J., Bullock J. S., Boylan-Kolchin M., Elbert O. D., Garrison-Kimmel S., Hopkins P. F., Kereš D., 2015, MNRAS, 453, 1305

White S. D. M., Frenk C. S., 1991, ApJ, 379, 52

White S. D. M., Rees M. J., 1978, MNRAS, 183, 341

Widrow L. M., Dubinski J., 2005, ApJ, 631, 838

Yozin C., Bekki K., 2015, MNRAS, 453, 2302

Zentner A. R., Kravtsov A. V., Gnedin O. Y., Klypin A. A., 2005, ApJ, 629, 219

APPENDIX A: SUPPLEMENTARY FIGURES

Here we present supplementary figures that are referenced in the main text.

A1 Simple χ^2-like for the 2D comparisons

In addition to the Monte Carlo sampling performed in Section 4.6.1, we sought a simpler method to gauge which simulation snapshot, or set of initial conditions, best matches the observed V_Z–Y and Z–Y positions of the satellites. We began by finding the continuous series of points in both planes which are the coordinates close to the centre of the turquoise band of sub-subhaloes. These were selected by finding the highest density of points along the x-axis (either the V_Z- or Z-coordinate) at every 5 kpc in the Y-coordinate (see the black lines in Figs 9 and 10). For each satellite position $(V^j_{z;\text{sat}}, Y^j_{\text{sat}})$, there is a coordinate $(V^j_{z_p}, Y^j_p)$, which is a point on the black line of Fig. 9 (or 10 for the Z–Y plane), that minimises the 'distance', $\lambda_{V_Z,Y} = \sqrt{(\frac{\Delta V_Z}{1\,\text{km s}^{-1}})^2 + (\frac{\Delta Y}{1\text{kpc}})^2}$ to the satellite. Of course, the weighing of the two coordinates, V_Z and Y, is important, but since Y spans roughly 300 kpc and V_Z spans roughly 500 km s^{-1}, we simply chose to weigh by 1 kpc and 1 km s^{-1}. Crucially, the path of the turquoise band changes depending on the initial conditions.

To give a rough estimate of which set of initial conditions and which orbital scenario (1 or 2) gives the better match to the observed satellites in the V_Z–Y plane, we computed a figure of merit $\epsilon_{V_Z,Y}$ which is calculated by taking each observed satellite in turn and counting how many sub-subhaloes, n_i, are in a thin bar of 10 kpc thickness between it and the point $(V^j_{z_p}, Y^j_p)$ – that was determined above using the minimum distance criterion – on the black line in Fig. 9, and how many are beyond it, called n_o. We use this to find the
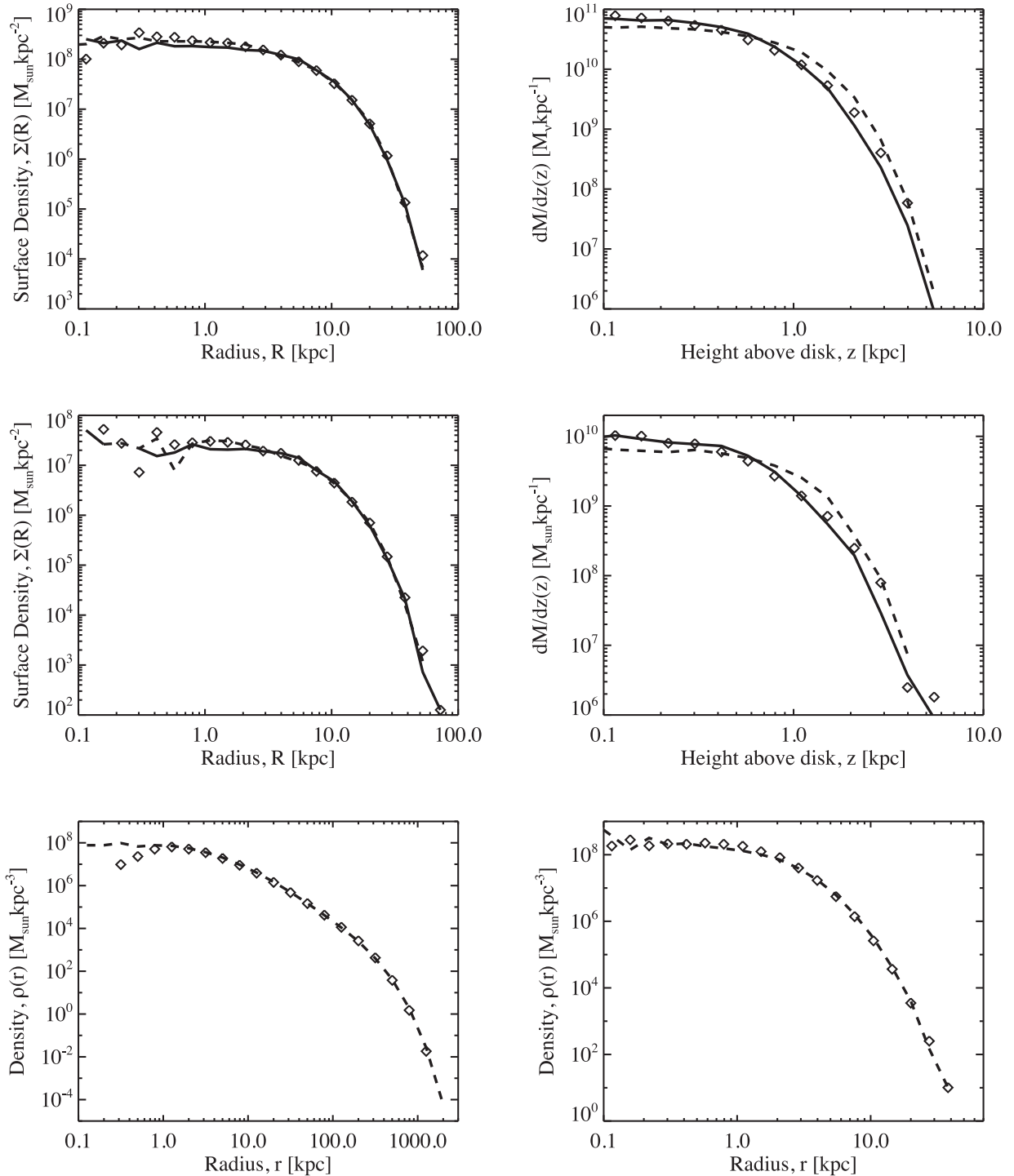
Figure A1. Density profile evolution over 10 Gyr for the four mass components of M31. The top two panels show the stellar disc, where the left-hand panel is the face-on surface density as a function of radius and the right-hand panel is the edge-on vertical mass gradient. The symbols show the initial, analytic density and the dashed lines show the density after 10 Gyr. Some panels have solid black lines which show the density after 1.5 Gyr. The second row shows the same, but for the gaseous disc. The bottom-left panel is the dark matter density and the bottom-right is the bulge density.

χ^2 of that point from the inverse error function of $\sqrt{2}\mathrm{erf}^{-1}(\frac{n_o}{n_o+n_i})$. We square and sum this quantity over all 13 satellites and divide by 13 and take the square root. This should give an indication of the probability of finding a satellite at a certain separation from the turquoise band.

In Fig. A6, we plot the variation of $\epsilon_{V_Z,Y}$ for the reference simulation with time near pericentre with black lines that correspond to

the left-hand y-axis. We do this for both scenario 1 (solid line) and 2 (dashed line). For both scenarios, there is a factor of 2 improvement at pericentre over the original value.

We computed another figure of merit which was again based on the mean path of the simulated sub-subhaloes in the Z–Y plane (the black line in Fig. 10). We call this $\epsilon_{Z,Y}$, but adopted a different approach because of the larger potential uncertainty in the Z
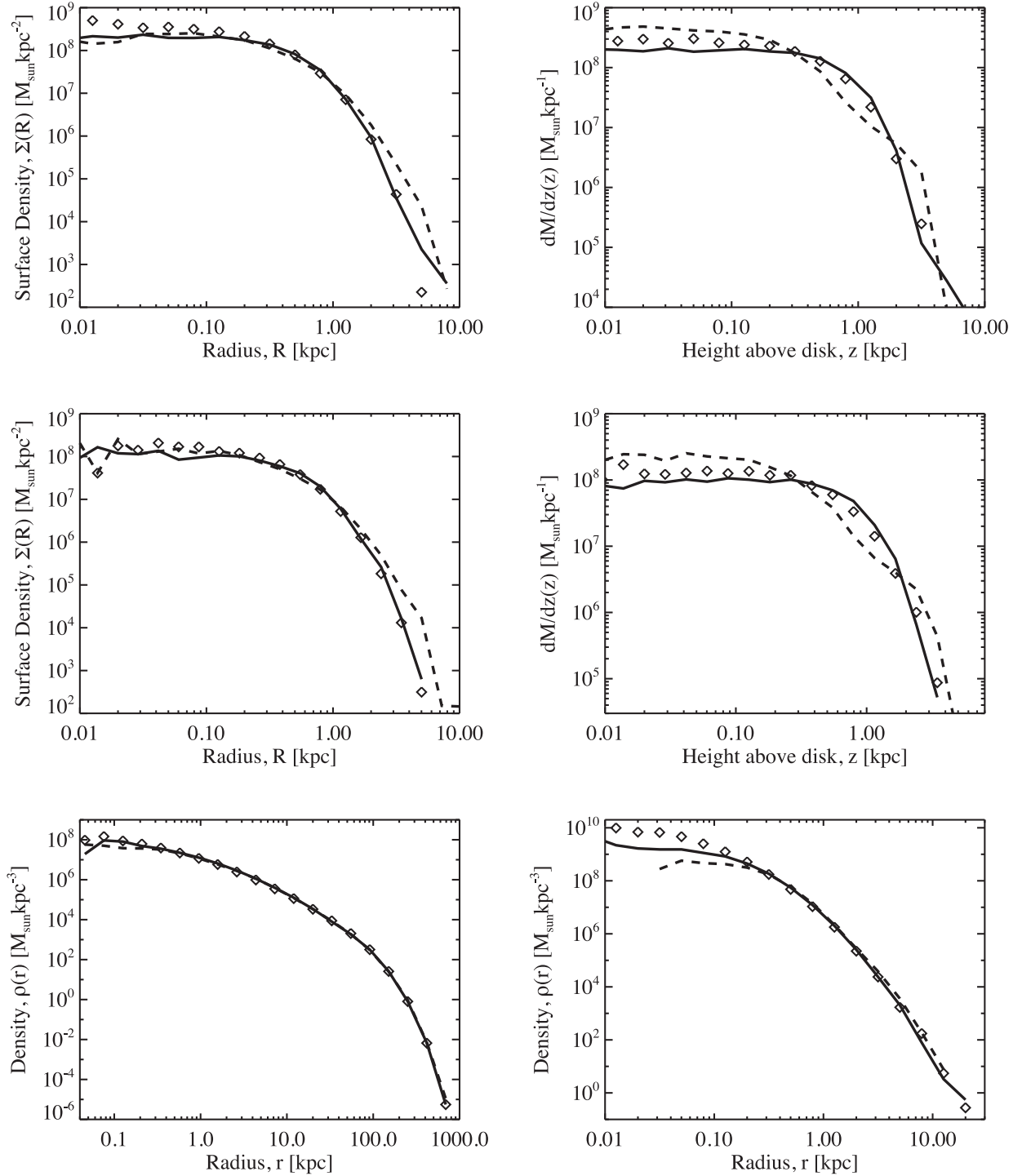
Figure A2. Density profile evolution over 10 Gyr for the four mass components of NGC 205. Panels, lines and symbols as per Fig. A1.

measurements for each satellite. First, we find the point (Z_p^j, Y_p^j) on the black line which has the same Y-coordinate as the satellite position (Z_{sat}^j, Y_{sat}^j) and then we compute the variance of Z_p from Z_i based on the uncertainty of Z_i i.e. $(\frac{Z_p^j - Z_{sat}^j}{\sigma_{Z_{sat}^j}})^2$. We sum these values for all 13 satellites, then divide by 13 and take the square root. We also plot the variation of $\epsilon_{Z, Y}$ with time in Fig. A6 with blue lines corresponding to the right-hand y-axis. Scenario 2 (dashed line) seems to be slightly more consistent with the distribution of the satellites in this plane.

For the two panels of Fig. A7 which show $\epsilon_{Z, Y}$ and $\epsilon_{V_Z, Y}$, we use black for scenario 1 and red for scenario 2. There is little improvement from scenario 1 to 2 as long as the initial tangential velocity is less than 50 km s^{-1}. An initial tangential velocity of 50 km s^{-1} or greater for scenario 1 is disfavoured. From the right-hand panel, there is a slight preference for scenario 2, especially for larger pericentres. However, for scenario 1, most pericentres are consistent with even the most stringent distance uncertainties for NGC 205. For scenario 2, the larger the pericentre, the more tension there is with the measured distance and its reliability.
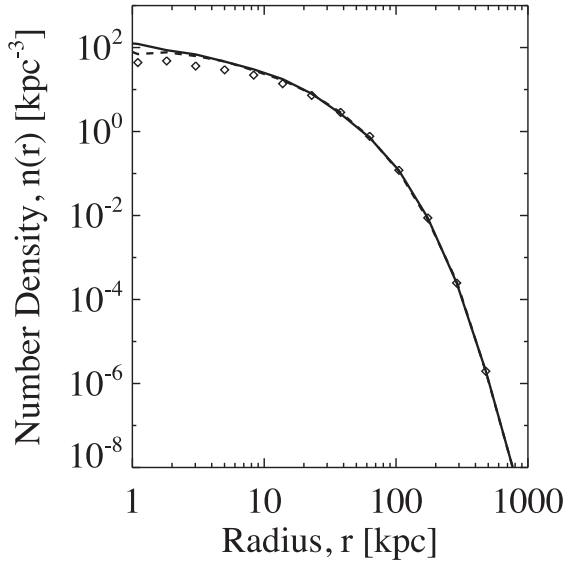
Figure A3. Number density evolution over 10 Gyr of the sub-subhalo distribution surrounding NGC 205. Lines and symbols as per Fig. A1.
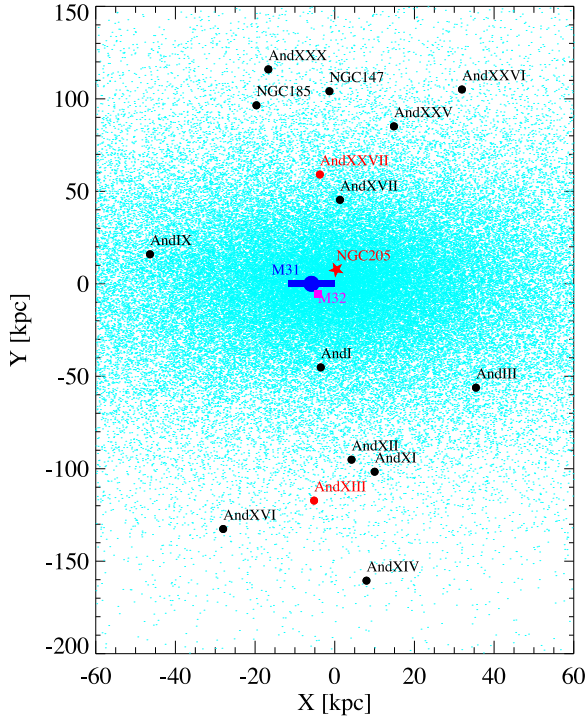

Figure A5. As per Fig. 9, but for the initial distribution of sub-subhaloes.
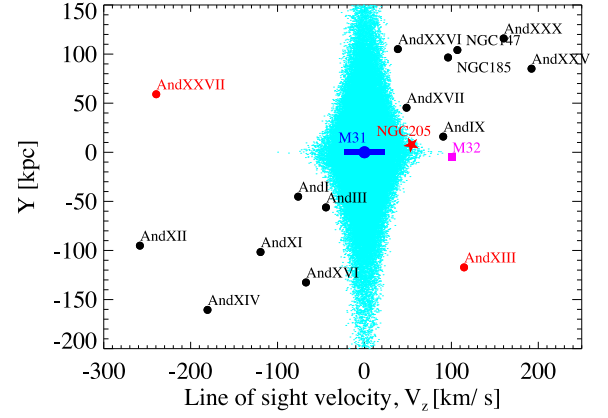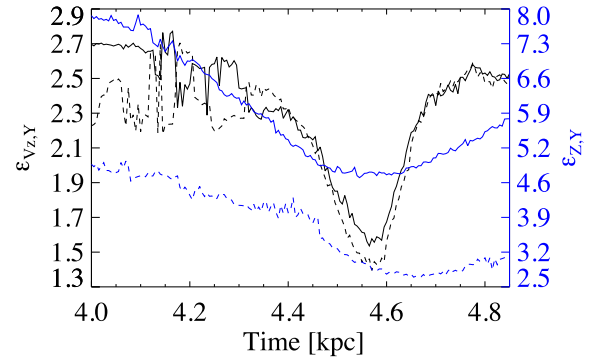

Figure A6. The black lines, which correspond to the left-hand y-axis are the χ^2-like figures of merit discussed in Section A1 for the match between the observed satellites and simulated sub-subhaloes in the V_Z–Y plane. The blue lines, which correspond to the right-hand y-axis are similar figures of merit for the Z–Y plane. The solid lines refer to scenario 1 and the dashed lines to scenario 2.
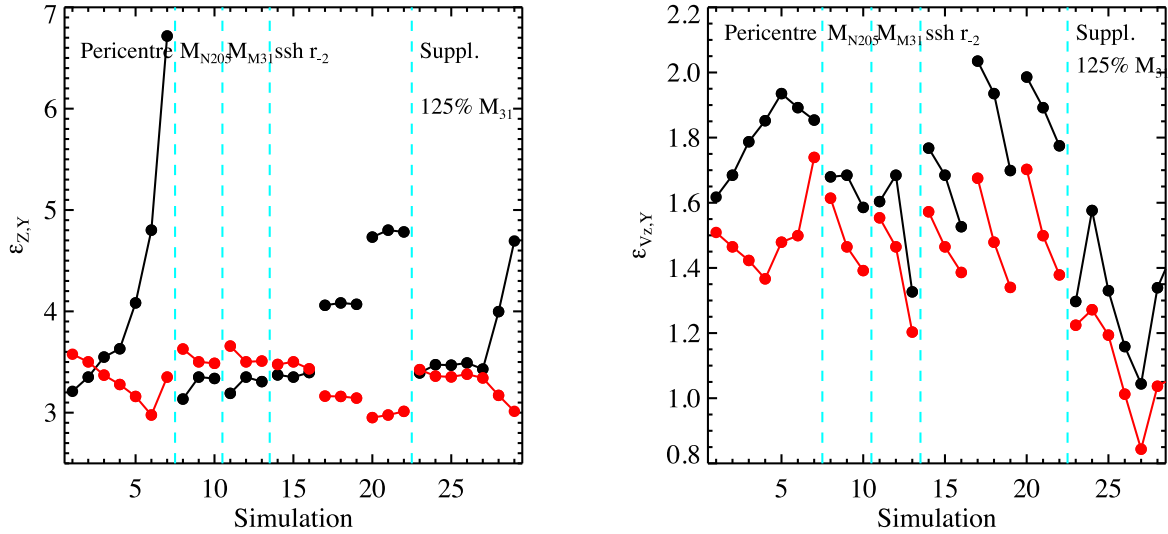

Figure A4. As per Fig. 5, but for the initial distribution of sub-subhaloes.

Figure A7. These two panels show the variations, across our series of simulations listed in Table 2, in our χ^2-like parameters found near pericentre for the distribution of simulated sub-subhaloes relative to the observed satellites in the Z–Y plane (left-hand panel) and the V_Z–Y plane (right-hand panel) as initially discussed in Section A1 and further discussed in Section 4.5. The black lines and symbols refer to scenario 1 and the red to scenario 2. The turquoise lines isolate related simulations to show the influence of (typically) a single parameter.

This paper has been typeset from a TEX/LATEX file prepared by the author.